International Journal of Hydrogen Energy 58 (2024) 1526–1540

Contents lists available at ScienceDirect

International Journal of Hydrogen Energy

journal homepage: www.elsevier.com/locate/he

Performance of $NiAl_2O_4$ spinel derived catalyst + dolomite in the sorption enhanced steam reforming (SESR) of raw bio-oil in cyclic operation

Leire Landa *, Aingeru Remiro, José Valecillos, Beatriz Valle, Javier Bilbao, Ana G. Gayubo

Department of Chemical Engineering, University of the Basque Country (UPV/EHU), P.O. Box 644, Bilbao, 48080, Spain

ARTICLE INFO

Handling Editor: Dr A Bhatnagar

Keywords:
SESR
Bio-oil
Hydrogen
Ni spinel
Coke
Reaction-regeneration cycles

ABSTRACT

The production of H_2 from raw bio-oil with high yield and purity requires the development of reforming technologies with low energy requirements, minimized CO_2 emissions, and stable and regenerable catalysts. This work studies the performance (activity, selectivity, stability and regenerability) in the sorption enhanced steam reforming (SESR) of raw bio-oil of a catalyst prepared by reduction of a $NiAl_2O_4$ spinel together with dolomite as CO_2 sorbent. The reaction runs were carried out in a fluidized-bed reactor under the following conditions: 550–700 °C; space time, 0.15 and 0.30 $g_{catalyst}{\cdot}h/g_{oxygenates}$; dolomite/catalyst mass ratio, 10 and 20; steam/carbon (S/C) molar ratio, 3.4; time on stream, 50 and 300 min. The highest H_2 yield (>92 %) and purity (>99 %) in the CO_2 capture period are obtained in the 600–650 °C range and with a dolomite/catalyst mass ratio of 10, due to synergy between catalyst and sorbent activity. The catalyst/sorbent system can be regenerated (4 h in air at 850 °C and subsequent reduction at 900 °C) and used in the successive reaction-regeneration cycles. The results are of relevant interest to progress towards scale-up of this process, which combines sustainable production of high purity H_2 from biomass with CO_2 capture.

1. Introduction

The production of renewable hydrogen is a priority goal in the global economic and political strategies for carbon neutrality and for a rapid transition to clean energy [1]. Hydrogen is a clean energy carrier, with a great potential to meet growing demand in the transport, industrial and power generation sectors. It is also a raw material in growing demand for fertilizer production, and its availability is key to the feasibility of producing fuels and synthetic commodities (such as methanol, dimethyl ether, olefins, aromatics or fuels) from CO_2 [2,3]. It is also important as a buffer to non-dispatchable renewable energy (wind, solar) [4].

The establishment of the H_2 economy through electrolysis technologies requires a huge multidisciplinary effort, including the application of advanced technologies, the development of stable and regenerable catalysts and advanced materials (nanostructured and composites) for H_2 production [5] and storage [6–10], combined with the efficient use of renewable energy [11]. In the transition period before the availability of green H_2, the production of H_2 from lignocellulosic biomass is of interest [12,13]. The cost of H_2 production from biomass with different technologies is higher than that of methane steam reforming [14], but emission taxes and CO_2 capture and storage costs are lower [13]. Among the different technologies, steam reforming (SR) of bio-oil is an alternative to pyrolysis/gasification of biomass and *in-line* SR of volatiles [15,16]. Sorption Enhanced Steam Reforming (SESR) of bio-oil has great appeal for avoiding CO_2 emissions through its in situ capture [17–19] and produces H_2 of higher purity than in SR. Bio-oil is obtained from fast pyrolysis of lignocellulosic biomass with a high yield, its production can be carried out off-site, with simple technologies and reduced environmental impact [20] and its transport to the valorization unit (for its large-scale reforming) is easier than that of the original biomass. The SR or SESR of bio-oil avoids the costly elimination of the high water content required for its use as a fuel or for hydrocarbon production [21], and the by-product handling required in the separation of some of its oxygenates compounds [22]. The overall reaction for SR or SESR of bio-oil involves the reforming reaction to produce (CO + H_2) (Eq. (1)) and the subsequent water-gas-shift (WGS) reaction (Eq. (2)):

$$C_nH_mO_k + (n\text{-}k)H_2O \rightarrow nCO + \left(n + \frac{m}{2}\text{-}k\right)H_2 \quad (1)$$

$$CO + H_2O \leftrightarrow CO_2 + H_2 \quad (2)$$

Thus, the overall equation is:

* Corresponding author.
E-mail address: leire.landa@ehu.eus (L. Landa).

https://doi.org/10.1016/j.ijhydene.2024.01.228
Received 18 October 2023; Received in revised form 3 January 2024; Accepted 20 January 2024
Available online 3 February 2024

$$C_nH_mO_k + (2n\text{-}k)H_2O \rightarrow nCO_2 + (2n + \frac{m}{2}\text{-}k)H_2 \quad (3)$$

H_2 yield is also affected by secondary reactions such as decomposition/cracking (Eq. (4)), reforming of decomposition products (CH_4 and hydrocarbons, Eqs. (5) and (6), respectively), and interconversion of oxygenates (Eq. (7)).

$$C_nH_mO_k \rightarrow C_xH_yO_z + \text{gas}\ (CO, CH_4, CO_2, C_aH_b, H_2, \ldots) + \text{coke} \quad (4)$$

$$CH_4 + H_2O \leftrightarrow CO + 3H_2 \quad (5)$$

$$C_aH_b + aH_2O \rightarrow aCO + (a + b/2)H_2 \quad (6)$$

$$C_nH_mO_k \rightarrow C_xH_yO_z \quad (7)$$

Moreover, the reactions of coke (C) formation and gasification (Eqs. (8)–(10)) should be considered as they affect catalyst stability.

$$\text{Methane decomposition, } CH_4 \rightarrow 2H_2 + C \quad (8)$$

$$\text{Boudouard reaction, } 2CO \leftrightarrow C + CO_2 \quad (9)$$

$$\text{Coke gasification, } C + H_2O \rightarrow CO + H_2 \quad (10)$$

Using a sorbent (taking CaO as example), the CO_2 is retained as:

$$CaO + CO_2 \leftrightarrow CaCO_3 \quad (11)$$

The existence of this reaction (Eq. (11)) in the SESR process, in addition to avoiding CO_2 emissions (with the consequent reduction of CO_2 separation and storage costs compared to the SR process), offers the following advantages over the SR process: i) improves the H_2 yield and selectivity by shifting the equilibrium of the WGS reaction (Eq. (2)), producing H_2 of higher purity; ii) reduces the energy requirement (since the decarbonation reaction is exothermic); iii) decreases the reaction temperature, thus reducing catalyst sintering (a critical factor in its selection). The release of high purity CO_2 in the regeneration of the sorbent by calcination (reverse of Eq. (11)) will facilitate its capture and subsequent valorization. A detailed review of sorbents has been carried out by Dou et al. [23], with calcium-based sorbents being the most widely used [24]. The high CO_2 sorption capacity at high temperatures and the low cost of CaO (easily prepared from limestone) make its use more interesting than that of alkaline ceramic sorbents (such as Li_2ZrO_3). The problem of losing CaO sorption capacity during cyclic carbonation/decarbonation operation has been addressed by incorporating CaO into other support materials and reactivating it with different thermal and chemical treatments [25].

SESR has been studied mainly for methane (SE-SMR process) [24–27], which is considered to be a more efficient technology than the combination of steam reforming of methane (SRM) and carbon capture and storage (CCS) units, commercially developed for blue H_2 production [28]. Using Ni and CaO based solids, SE-SMR is preferentially operated around 650 °C, at atmospheric pressure and with the S/C (steam/carbon) molar ratio in the range of 3–4 [29]. Under these conditions, H_2 purity of over 95 % (dry basis) is achieved, compared to 76 % in SR. The scale-up of the process is studied by simulation with a dual fluidized-bed system combining a reformer and a calciner with catalyst circulation between the two units [30]. Thus, the activity of the sorbent is recovered in the calciner and the homogeneous temperature in each unit (higher in the calciner unit) favors its control and that of the heat transfer of the catalyst/sorbent stream (key to minimize the external energy input).

Due to the complexity of bio-oil (a mixture of oxygenates of different nature) and its handling, SESR has generally been studied for pure model compounds, such as acetic acid [31–35], ethanol [36,37], phenol [38,39], glycerol [40,41] and toluene [42], and for mixtures of oxygenates [32,43]. In general, Ni-based catalysts have been used with different materials containing CaO as CO_2 sorbent, and also bifunctional composites (usually based on Ni over CaO and with different modifications) have been used [36,44–47]. The objectives of these works have focused on the optimization of the catalyst composition and the reaction conditions, although the results are different and the appropriate conditions to obtain a H_2 purity above 95 % depends on the nature of the oxygenates. Thus, this nature has a great influence on the stability of the catalysts, which has also been established in the SR of oxygenates in bio-oil [48].

Experimental studies on the SESR of the aqueous fraction of bio-oil are very scarce [49–51]. Remiro et al. [50], using a Ni/La_2O_3–Al_2O_3 catalyst and calcined dolomite as sorbent, observed a significant role of the catalyst/sorbent mass ratio due to the active role of dolomite for oxygenates cracking and also for reforming reactions. A suitable balance was stricken at 600 °C for catalyst/dolomite mass ratios $\geq$0.17 with a H_2 yield around 99 %. The SESR of raw bio-oil offers a higher yield referred to biomass, as established by thermodynamic studies [52] and experimentally [35,53]. Landa et al. [53] obtain high H_2 purity using Ni/Al_2O_3 (obtained by reduction of a $NiAl_2O_4$ spinel) as catalyst and dolomite as sorbent, with better performance than other catalyst + sorbent systems, such as Ni/CeO_2+dolomite or Ni/Al_2O_3+CaO/mayenite. Iliuta et al. [54] also determine the lower catalyst deactivation in SESR of bio-oil compared to SR by simulating the process in a packed-bed reactor, using the kinetic model of Gayubo et al. [55] for the reactions involved in SR of bio-oil (on a Ni/La_2O_3-αAl_2O_3 catalyst) and the kinetics of CO_2 adsorption over Li_2CuO_2.

Considering the interest of activity recovery by catalyst regeneration for the viability of the SESR process, Acha et al. [43] have verified the importance of the Ni catalyst support and the composition of the dolomite used as sorbent for the activity recovery of both materials used in the SESR of acetic acid and a mixture of oxygenates. The results highlight the importance of a support that minimizes sintering and coke deposition, while dolomites lose their capture capacity upon reactivation. Li et al. [35] investigated the stability of a Ni/$Ce_{1.2}Zr_1Ca_5$ bifunctional catalyst-sorbent (Ce/Ca ratio of 0.24) in the SESR of acetic acid and poplar sawdust pyrolysis oil in a packed-bed reactor over 15 reaction-regeneration cycles. While an excellent catalytic performance was reported after 15 consecutive cycles for the SESR of acetic acid (550 °C, S/C of 4 and LHSV of 0.48 ml/$g_{catalyst}$·h), a decrease in CO_2 adsorption capacity and H_2 yield was observed in the SESR of bio-oil, which was explained by the sintering of CaO particles and the formation of coke and sintering of Ni. These phenomena were more important in the bio-oil SESR, with the formation of more condensed coke, whose removal by gasification (Eq. (10)) is not complete at the reactivation conditions (750 °C).

Considering the literature background and our above-mentioned previous results, the attention of this manuscript has been focused on the performance of the catalyst/sorbent system of (Ni/Al_2O_3 catalyst derived from $NiAl_2O_4$ spinel) + dolomite in the SESR of raw bio-oil operating in reaction-regeneration cycles. The process addresses the gaps in H_2 production from biomass using bio-oil without pre-treatment, producing high purity H_2, no CO_2 emissions and lower energy requirements than other reforming processes. The catalyst was selected due to its complete regenerability in the SR of raw bio-oil under suitable conditions [56]. Likewise, dolomite, besides being a low-cost material, has a good performance as a CO_2 sorbent, with a positive synergy with Ni/Al_2O_3 catalyst derived from $NiAl_2O_4$ spinel in the SESR of bio-oil and as guard-bed, retaining a fraction of the deposited coke [57]. Furthermore, the valorization of raw bio-oil (with the attraction of high H_2 yield) and the low temperature required to favor the extent of CO_2 adsorption have the drawback of high coke deposition, leading to rapid catalyst deactivation, which is a challenge for catalyst and sorbent reactivation. Consequently, given the importance of deactivation, special attention has been paid to the study of its causes and mechanism, using several characterization techniques (Temperature Programmed Oxidation (TPO), adsorption-desorption of N_2, Temperature Programmed Reduction (TPR), X-Ray Diffraction (XRD), Scanning Electron Microscopy (SEM) and X-Ray Photoelectron Spectroscopy (XPS)).

The results in this manuscript are explained by considering the effect

of the reaction conditions on the extent of each reaction involved in the SESR process and on the content and nature of the coke deposited on the catalyst. These results show that SESR of raw bio-oil is an attractive route for the production of H_2 from biomass, avoiding the CO_2 emissions associated with other reforming technologies. Furthermore, the progress in knowledge of the process corresponds to key objectives for its viability, such as the use of raw bio-oil as feedstock, the proposal of a highly active catalyst with moderate deactivation by coke and regenerable, and the establishment of optimal conditions (reaction temperature, sorbent/catalyst mass ratio, space-time) for maximizing H_2 yield and purity and for stable operation in SESR of bio-oil in successive reaction-regeneration cycles. The use of a low-cost sorbent such as dolomite is another factor favoring the feasibility of the process. In addition, the results are based on experiments in a fluidized-bed reactor, which favors its use in scale-up where this type of reactor is likely to be required.

2. Experimental

2.1. Bio-oil

The raw bio-oil was supplied by BTG Bioliquids BV (The Netherlands) and was synthetized by fast pyrolysis of pine sawdust in a plant with a capacity to operate continuously with 5 ton/h of biomass (bio-oil yield of 70 %) and with a conical rotatory reactor. The physicochemical properties of the bio-oil are as follows: water content, determined by Karl-Fischer titration (KF-Titrino Plus 870), 24 wt%; density, 1.201 g/ml; viscosity at 40 °C, 250 cP (*Brookfield DV2T Ametek);* pH, 2.5–3.5, and; empirical formula, obtained by CHO analysis, using a Leco CHN-932 analyzer (water-free basis), resulted in $C_{4.6}H_{6.2}O_{2.4}$. The detailed composition of the raw bio-oil was determined using a Shimadzu QP2010S gas chromatography/mass spectrometer (GC/MS) equipped with a BPX-5 column (50 m × 0.22 mm × 0.25 μm) and mass-selective detector. The main compounds are ketones, acids, phenols (guaiacol), esters, saccharides (levoglucosan), aldehydes, furans/furanones, alcohols, and ethers (Table 1).

2.2. Preparation of catalyst and sorbent

The $NiAl_2O_4$ spinel (33 wt% nominal Ni content) was synthesized by the co-precipitation method [58], mixing at 25 °C aqueous solutions of hexahydrated nickel nitrate ($Ni(NO_3)_2{\cdot}6H_2O$, Scharlau, purity of 98 %) and nona-hydrated alumina nitrate ($Al(NO_3)_3{\cdot}9H_2O$, Honeywell Fluka, purity of 98 %) and adding dropwise a 0.6 M solution of ammonium hydroxide (NH_4OH 5 M, Honeywell Fluka) as a precipitating agent until a pH of 8 is reached. The precipitate was then recovered by filtration and washed with distilled water to remove the remaining ammonium ions, dried overnight at 110 °C, calcined (850 °C for 4 h, with a heating ramp of 10 °C/min), crushed and sieved to obtain particle sizes in the range of 150–250 μm. The $NiAl_2O_4$ spinel precursor was reduced (conditions indicated in Section 2.4) in order to obtain the Ni/Al_2O_3 catalyst active for the reforming reactions. A schematic of the catalyst synthesis process is shown in Fig. S1.

Table 1
Composition (wt%) of raw bio-oil obtained from fast pyrolysis of pine sawdust.

Compound	wt%
Acids	19.5
Acetic acid	16.6
Ketones	21.4
Linear	*17.1*
Acetone	5.2
Acetol	9.4
Cyclic	*4.3*
Esters	11.3
Furans/Furanones	5.0
Alcohols	3.2
Aldehydes	6.8
Ethers	0.8
Saccharides	13.7
Levoglucosan	11.1
Phenols	18.4
Alkylphenol	1.4
Guaiacol	11.1
Catechol	0.9
Syringol	0.5
Others	4.5

Calcined dolomite, composed of calcium and magnesium oxide (CaO and MgO), is obtained from dolomitic minerals consisting of calcium and magnesium carbonate ($CaMg(CO_3)_2$) with Fe_2O_3 impurities (supplied by Calcinor S.A. (Cantabria, Spain)) through a calcination process (Eq. (12)).

$$CaMg(CO_3)_2 + \text{heat} \leftrightarrow CaO + MgO + 2CO_2 \quad (12)$$

The preparation of the sorbent consists of a first grinding to adjust the particle size between 90 and 125 μm. Then, the natural dolomite is dried at 110 °C for 24 h. Finally, it is calcined at 850 °C for 5 h with a heating rate of 10 °C/min, so that the natural sorbent is thermally decomposed into CaO (the active phase for CO_2 adsorption) and MgO [59,60]. Afterwards, it is sieved again to ensure a particle size between 90 and 125 μm, since during the calcination step the particles decrease in size due to decrepitation caused by the loss of CO_2 from the carbonates. A schematic of the calcined dolomite preparation procedure is shown in Fig. S2. Note that the particle size of the dolomite is different from that of the catalyst to facilitate their separation by sieving after each reaction, so that the catalyst used can be characterized separately from the sorbent (and also from the inert solid used in the fluidized-bed reactor, as described in Section 2.4).

2.3. Characterization of the catalyst

The physical properties of the fresh-reduced and used catalysts (BET surface area, pore volume and mean pore diameter), were characterized by adsorption-desorption of N_2 in a Micromeritics ASAP 2010. Temperature Programmed Reduction (TPR) analysis was carried out in a Micromeritics AutoChem II 2920 apparatus for determining the reducibility of the metal species. The TPR measurement was also used to estimate the real Ni content in the spinel and after catalyst regeneration using a thermobalance (TA Instruments SDT-2960) to determine the O atoms removed as H_2O. The structural properties of fresh-reduced and used catalyst were analyzed by X-Ray Diffraction (XRD), measured on a Bruker D8 Advance diffractometer with CuKα1 radiation, in order to calculate the sintering dynamics of the Ni crystals (using the Scherrer equation) and the crystalline state of the coke deposits. The amount and nature of coke deposited on used catalyst samples has been determined by Temperature Programmed Oxidation (TPO) in a TA-Instruments TGA-Q5000IR thermobalance, coupled in line with a mass spectrometer (Thermostar Balzers instrument) to monitor the CO_2 signal. The coke content has been quantified from the CO_2 spectroscopic signal, since the oxidation of Ni crystals during the combustion process could mask the thermogravimetric signal. The surface mass content of the different elements on the catalyst surface and the possible migration of Ni during the deactivation or regeneration stages has been determined by X-Ray Photoelectron Spectroscopy (XPS) analysis in a SPECS system equipped with a Phoibos 150 1D-DLD analyzer, Al Kα monochromatic radiation (1486.6 eV), an X-ray exciting source and a hemispherical electron analyzer. The binding energy of the C1s carbon peak was set at 284.6 eV to correct the material charging, and the analysis was carried out using an electron take off angle of 90°. The scanning electron microscopy (SEM) images of the used catalysts were obtained in a Hitachi S-4800 N field emission gun scanning electron microscope with an accelerating voltage of 5 kV and a secondary electron detector (SE - SEM).

2.4. Reaction equipment and operating conditions

The kinetic runs have been performed in an automated reaction system (MicroActivity-Reference, PID Eng & Tech) provided with two units (thermal step and catalytic step) in series (Fig. S3 in Supplementary Material). The first unit (thermal treatment) consists of a U-shaped steel tube (inner diameter = 0.75 in) at 500 °C for controlled vaporization of bio-oil and repolimerization of some oxygenates (mainly phenolic compounds) which are retained as a carbonaceous solid called pyrolytic lignin (PL) [50]. In this way, the subsequent catalyst deactivation in the SESR and SR processes is attenuated, with a moderate decrease in the flow rate of oxygenates entering the catalytic reactor (unit 2). The volatile stream leaving the thermal treatment unit is converted (by catalytic SESR or SR) in a fluidized-bed reactor (stainless steel, with 22 mm of internal diameter and total length of 460 mm). In this reactor, the catalytic bed composed of $NiAl_2O_4$ spinel (with a particle size of 150–250 μm) and sorbent (calcined dolomite, with a particle size between 90 and 125 μm) is mixed with inert solid (SiC, with a particle size of 75 μm) in order to improve the fluid dynamics of the bed. The inert nature of SiC in the SR of bio-oil has been demonstrated in a previous work [53].

An injection pump (*Harvard Apparatus 22*) was used to feed the bio-oil (0.06 ml/min) and a *307 Gilson pump* to co-feed the additional water required according to the desired steam to carbon (S/C) molar ratio. The reaction products were analyzed in a Micro GC (*Varian CP-490*) connected in-line to the reactor through an insulated line (130 °C) to avoid condensation of the products. The gas chromatograph is equipped with three analytical channels: molecular sieve MS5 for quantification of H_2, O_2, N_2, CH_4 and CO; PPQ column for light hydrocarbons (C_2–C_4), CO_2 and water; and Stabilwax for oxygenated compounds (C_{2+}) and water.

Prior to each reaction, the Ni spinel precursor is reduced in situ under H_2–N_2 (7 vol% H_2) at 850 °C for 4 h to obtain the active Ni/Al_2O_3 catalyst with the Ni metallic phase well-dispersed on the alumina support [58]. The SESR runs of raw bio-oil were carried out in the catalytic reactor under the following conditions: 550–700 °C; bio-oil flow rate, 0.06 ml/min; space time, 0.15 and 0.30 $g_{catalyst}{\cdot}h/g_{oxygenates}$ (corresponding to 0.5 g and 1 g of catalyst, respectively); sorbent/catalyst mass ratio, 10 and 20; steam/carbon (S/C) molar ratio at the reactor inlet, 3.4; time on stream (TOS), 50 and 300 min. Joint regeneration conditions of catalyst and dolomite were: 850 °C in air in an external oven, for 4 h.

2.5. Reaction indices

The following reaction indices were used to quantify the results:

The conversion of oxygenates in the treated bio-oil (that is, the volatile oxygenates exiting the Unit 1 used for thermal treatment) is expressed as the carbon units converted into gas:

$$X = \frac{F_{out,gas}}{F_{in}} \tag{13}$$

where $F_{out,gas}$ is the carbon-molar flow rate of the total carbon in gaseous product (CO_2, CO, CH_4 and light hydrocarbons) at the reactor outlet, and F_{in} is the carbon-molar flow rate of the oxygenates at the reactor inlet. Eq. (13) is suitable for quantifying the total conversion of oxygenates in the reforming reactor because the yield of solid carbon (coke) is low under the conditions studied (below 5 % as defined in the following Eq. (15)).

$$H_2 \text{ yield is calculated as : } Y_{H_2} = \frac{F_{H_2}}{F^{o}_{H_2}} \tag{14}$$

where F_{H2} is the H_2 molar flow rate in the product stream and $F^{o}_{H_2}$ is the stoichiometric molar flow rate, calculated as $(2n + m/2 - k)/n\ F_{in}$, according to the global stoichiometry for bio-oil ($C_nH_mO_k$) steam reforming (including the WGS reaction) (Eq. (3)).

$$\text{Yield of the carbon products : } Y_i = \frac{F_i}{F_{in}}\ (i = CO, CO_2, CH_4 \text{ and HC}) \tag{15}$$

where F_i is the carbon-based molar flow rate of the i-product (CO, CO_2, CH_4 and HC) in the effluent (out) stream of the second unit (catalytic reactor).

3. Results

3.1. Behavior of catalyst/sorbent under different conditions

This section shows the results of the effect of different operating variables on the reaction indices in the SESR of bio-oil, both in the CO_2 capture period and after dolomite saturation, in order to analyze the activity and stability of the catalyst/sorbent system. The focus is on the effect of temperature, but the effect of sorbent/catalyst mass ratio and space time are also addressed, considering the relationship of the effect of these variables. The results shown in this section are mean values obtained from repeated experiments (with an average mean error below 5 %).

Fig. 1 compares the evolution with time on stream (TOS) of the reaction indices (conversion and product yield) for different temperatures in the 550–700 °C range, with a sorbent/catalyst mass ratio of 10 and a S/C ratio of 3.4. A low space time (0.15 $g_{catalyst}{\cdot}h/g_{oxygenates}$) was used to better appreciate the effect of temperature on catalyst stability in the post-saturation period. The results obtained in runs without sorbent (SR tests) and with a sorbent/catalyst mass ratio of 20 are shown in Figs. S4 and S5, respectively (Supplementary Material).

As observed in Fig. 1 and Fig. S5, the SESR process can be divided into three regions: pre-breakthrough (with CO_2 capture, green zone in Fig. 1c), breakthrough (when dolomite saturation begins to be noticeable, blue zone in Fig. 1c) and post-breakthrough (after complete saturation of the dolomite). Under the conditions of Fig. 1 (with a dolomite/catalyst mass ratio of 10), the duration of the pre-breakthrough period is about 30 min above 600 °C and is slightly longer at 550 °C (Fig. 1c). The duration of this period is doubled when twice the sorbent/catalyst ratio is used (Fig. S5). In the capture period, the higher H_2 yield and lower CO and CH_4 yields compared to the SR test (Fig. S4) are explained by the shift of the WGS reaction equilibrium by CO_2 capture (Eq. (2)) and, as a consequence, the shift of the SRM reaction equilibrium (Eq. (5)). The breakthrough period involves the depletion of the carbonation reaction efficiency, and therefore, a sudden increase in the yield of CO_2 (Fig. 1c and S5c) and a decrease in the yield of H_2 (Fig. 1b and S5b) is observed. In the post-breakthrough period, CO_2 removal is no longer effective and SR and WGS reactions occur together with other secondary reactions responsible for coke formation. Consequently, in this period, the reaction indices evolve with time on stream due to the deactivation of the catalyst and sorbent.

Fig. 2 compares the product distribution results in the CO_2 capture period of SESR reactions (for sorbent/catalyst mass ratio values of 10 and 20) and SR reactions (sorbent/catalyst mass ratio of 0) at different temperatures. The values of SESR reactions are mean values during the CO_2 capture period, whereas those of SR (with a noticeable deactivation, Fig. S4) correspond to zero time on stream. Light hydrocarbons yield is not shown because it is insignificant for all the operating conditions studied. In the SR reactions (solid lines in Fig. 2), the H_2 yield increases with increasing temperature (from 58 % at 550 °C to 81 % at 700 °C) because the reforming of oxygenates and CH_4 is favored. Consequently, the yield of CH_4 is negligible at 700 °C in Fig. 2. The CO yield increases with increasing temperature as a consequence of favoring the reverse-WGS reaction. In the SESR reactions (dashed and dotted lines in Fig. 2), temperature also affects the CO_2 adsorption equilibrium, which becomes unfavorable with increasing reaction temperature. In the range studied, the increase in temperature favors the formation of H_2, whose yield increases from 74 % to 92 % between 550 and 600 °C for a sorbent/

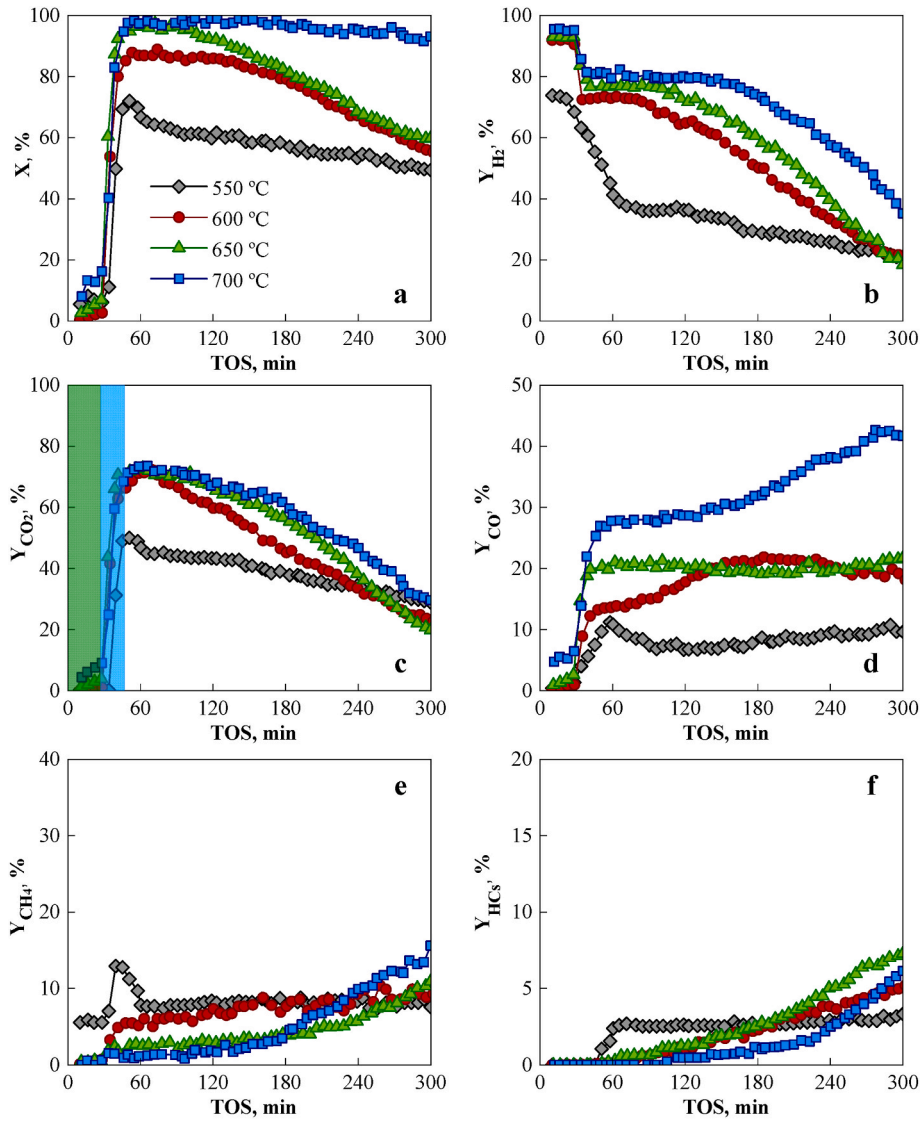

Fig. 1. Effect of temperature on the evolution with time on stream of conversion (a) and yields of H_2 (b), CO_2 (c), CO (d), CH_4 (e) and C_2–C_4 hydrocarbons (HCs) (f). Reaction conditions: space time, 0.15 $g_{catalyst}$·h/$g_{oxygenates}$; sorbent/catalyst mass ratio, 10; S/C, 3.4. Colored zones in graph c: CO_2 capture period (green shade) and breakthrough period (blue shade). (For interpretation of the references to color in this figure legend, the reader is referred to the Web version of this article.)

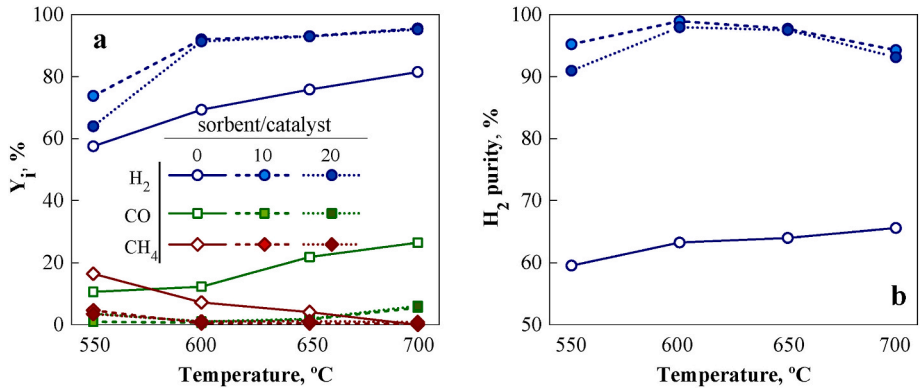

Fig. 2. Effect of temperature on product yield distribution (H_2, CO_2, CO and CH_4) (a) and H_2 purity (b) in the CO_2 capture period for different sorbent/catalyst mass ratio (0 (SR), 10, 20). Reaction conditions: space time, 0.15 $g_{catalyst}$·h/$g_{oxygenates}$; S/C, 3.4.

catalyst mass ratio of 10 (Fig. 2a). It is noteworthy that at 600 °C the reforming of CH_4 is almost complete with a yield of less than 1 %. Above this temperature, the yield of H_2 increases only slightly despite the increase in oxygenate conversion (Fig. S4a). This result is explained by the fact that CO_2 capture by dolomite is unfavorable above 600 °C [49]. Thus, at 650 and 700 °C, the sorbent capture capacity decreases slightly,

as observed in the pre-breakthrough period in Fig. 1c. Although dolomite promotes the formation of CH_4 by oxygenates cracking/decomposition reaction (Eq. (4)), the yield of CH_4 remains almost null in the CO_2 capture period above 600 °C due to the high activity of the Ni/Al_2O_3 catalyst for its SR at these temperatures [61]. Nevertheless, the CO yield (which is less than 1 % at 600 °C) slightly increases to 6 % at 700 °C with a sorbent/catalyst mass ratio of 10 due to the promotion of the reverse-WGS reaction with increasing temperature, which leads to a decrease in H_2 purity at high temperatures (Fig. 2b). For a sorbent/-catalyst mass ratio of 20 (dotted lines in Fig. 2), the product yields in the CO_2 capture period are almost equal to those obtained with a sorbent/catalyst mass ratio of 10, except at 550 °C. At this low temperature, the H_2 yield for a sorbent/catalyst mass ratio of 20 is only 64 % (slightly higher than that obtained in the SR test), which can be attributed to the significant deactivation of the catalyst along the CO_2 capture period in the SESR run with high dolomite loading, as observed in Figs. S5a–c. This catalyst deactivation is due to the activity of dolomite for decomposition/cracking of oxygenates [59], which is favored by the low extent of SR reactions at this low temperature for this low space time.

As mentioned above, the evolution of the product distribution with time on stream in the post-breakthrough period (after CO_2 capture) in Fig. 1 is a consequence of catalyst deactivation. Thus, the yields of H_2 and CO_2 decrease due to the attenuation of the SR and WGS reactions, which involves an increase in the yields of CO (Fig. 1d), CH_4 (Fig. 1e) and hydrocarbons (Fig. 1f). To explain the effect of temperature on these trends, it is necessary to take into account the different residual activity of the catalyst at the beginning of this period. Moreover, the relationship between the effects of temperature and oxygenate concentration on deactivation [62,63] and the role of dolomite on deactivation should be considered [50,53,57]. Thus, as mentioned above, at low temperature (550 °C) the catalyst has undergone significant deactivation during the CO_2 capture period because the space time was low to convert all the oxygenates, which explains the subsequent slow decrease in conversion (Fig. 1a) and yields of H_2 (Fig. 1b) and CO_2 (Fig. 1c), and the slow increase in CO yield (Fig. 1d). These trends indicate that the catalyst/sorbent system has reached a quasi-steady state at this temperature. Conversely, above 600 °C, the catalyst/sorbent system has a higher remaining activity after the CO_2 capture period and its deactivation in the post-breakthrough period is slightly more pronounced with increasing temperature, as observed by the faster decrease in H_2 yield with time on stream (Fig. 1b). The increase in the extent of decomposition/cracking reactions of oxygenates over dolomite (Eq. (4)) with increasing temperature contributes to the increase in the yield of carbonaceous products [59,60], which explains why the decay of oxygenates conversion with time (Fig. 1a) is less pronounced than the decrease in H_2 yield (Fig. 1b) at high temperature.

Comparing the results of Fig. 1 (corresponding to SESR with a sorbent/catalyst mass ratio of 10), Fig. S4 (SR) and Fig. S5 (SESR with a sorbent/catalyst mass ratio of 20), it is observed that the effect of temperature on catalyst stability depends on the presence and content of dolomite with the catalyst. Thus, at low temperatures (550–600 °C), the presence and content of dolomite has a negative effect, leading to a faster catalyst deactivation. At 650 °C, the presence and content of dolomite prolongs the stability period of the catalyst, but after this period, the deactivation is faster than in the SR process, with a rapid decrease in the reaction indices. Consequently, the H_2 yields at 300 min on stream at this temperature are 33 %, 20 % and 17 % for SR (Fig. S4b), sorbent/catalyst mass ratios of 10 (Figs. 1b) and 20 (Fig. S5b), respectively. On the contrary, at 700 °C, the moderate presence of dolomite (sorbent/catalyst mass ratio of 10) has a positive effect, with the reaction indices decreasing more slowly with time on stream. This result is explained by the activity of dolomite for SR reactions at this temperature, and also because dolomite deactivates more slowly than the catalyst [60]. However, for a sorbent/catalyst mass ratio of 20, there is a faster catalyst deactivation. In fact, the use of a high dolomite/catalyst ratio of 20 (Fig. S5) results in faster catalyst deactivation at all temperatures.

In addition to the variables studied above (reaction temperature and sorbent/catalyst mass ratio), the effect of space time has been studied, as the amount of available active catalyst sites influences the extent of reforming and WGS reactions, and consequently the distribution of products and catalyst deactivation. Fig. 3 shows the evolution of the reaction indices with time on stream for a high space time of 0.3 $g_{catalyst}{\cdot}h/g_{oxygenates}$ (twice that of Fig. 1). The results correspond to 600 °C and a sorbent/catalyst mass ratio of 10 (the conditions leading to the highest H_2 purity according to Fig. 2b). The duration of the CO_2 capture period in Fig. 3 (about 50 min) is longer than that obtained in Fig. 1 at the same temperature (about 30 min, red dots) due to the higher content of dolomite in the bed (10 g, compared to 5 g in Fig. 1). It should be noted that this dolomite content is the same as that used in the runs with a sorbent/catalyst mass ratio of 20 (Fig. S5), but now with twice the amount of catalyst. Comparing the product yields in the CO_2 capture period in Fig. 3 and the red curves in Fig. 1 (those corresponding to 600 °C with half the space time as in Fig. 3), a significant improvement in H_2 yield is observed with increasing space time, with a value of 95 % in Fig. 3 and almost the same H_2 purity (around 99 %) in both runs. The combined effect of increasing the CO_2 capture capacity by increasing the amount of dolomite and increasing the extent of reforming and WGS reactions by increasing the amount of catalyst contributes to this result. Furthermore, after the CO_2 capture period, it is observed that the stability of the catalyst has increased with increasing space time value. As a result, the H_2 yield remains high (about 72 %) after 5 h of operation, compared to about 25 wt% under the same conditions but with half the space time (red curve in Fig. 1b). This higher stability is consistent with previous studies on bio-oil SR, that show an improvement in catalyst stability with increasing space time values due to the lower concentration of oxygenates in the reaction medium, as a result of the higher extent of oxygenate reforming reactions [63,64].

3.2. Characterization of catalyst and sorbent used under different conditions

The results in section 3.1 show that the stability of the catalyst depends on the reaction conditions. In order to identify the causes responsible for the deactivation and its dynamics during the CO_2 capture periods in Fig. 1, samples of the catalyst used after 50 min on stream (end of the CO_2 capture period) and after 300 min on stream (end of the runs in Fig. 1, comprising the post-capture period) were analyzed using different techniques (TPO, TPR, XRD, N_2 adsorption-desorption and SEM). After each reaction, the three components of the catalytic bed (catalyst/sorbent/inert solid) were separated by sieving, in order to

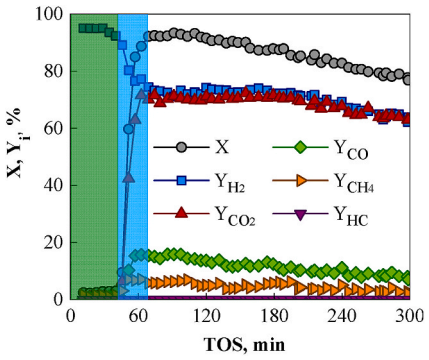

Fig. 3. Evolution with time on stream of carbon conversion and product yields. Reaction condition: 600 °C; space time, 0.3 $g_{catalyst}{\cdot}h/g_{oxygenates}$; dolomite/catalyst mass ratio, 10; S/C, 3.4. Colored zones: CO_2 capture period (green shade) and breakthrough period (blue shade). (For interpretation of the references to color in this figure legend, the reader is referred to the Web version of this article.)

characterize the used catalyst separated from the sorbent or inert solids.

3.2.1. Analysis of coke deposits

The Temperature Programmed Oxidation (TPO) of the used catalyst provides information on the total content of coke deposited, and the nature and/or location of the coke on the catalyst [63,65]. Fig. 4 shows the TPO profiles and the corresponding coke content (wt%) for the catalyst used at different temperatures. It should be noted that the scale of the two graphs is different. Graph (a) corresponds to the runs performed up to the breakthrough regime with CO_2 capture (50 min time on stream), whereas graph (b) corresponds to the catalyst used in the 300 min duration tests (corresponding to the reactions in Fig. 1). For comparison, the TPO profiles for the catalysts used in the SR tests (without sorbent) are plotted in Fig. S6. In line with previous results in the literature on coke deposition on supported Ni-based catalysts used in the SR of oxygenates and bio-oil [58,63,65], the TPO profiles in Fig. 4 show two different combustion domains, corresponding to coke burning below 500 °C or above 500 °C. These fractions can be attributed to the different nature of the coke: amorphous carbon (burning at low temperature) and carbon filaments or graphitic structures (burning at high temperature) [66,67]. It has also been claimed that the location of the combustion peaks depends on the location of the coke, with coke deposited on the metal surface burning at a lower temperature than coke deposited on the support [61,65].

The results in Fig. 4 reveal a remarkable effect of the reforming temperature on the coke content and nature in the two groups of runs. For the catalysts used only in the CO_2 capture period (Fig. 4a), the coke burning below 500 °C (presumably amorphous coke deposited on the Ni sites) is the only coke fraction at a reforming temperature of 550 °C. As the reaction temperature increases, the total coke content decreases and so does this amorphous coke fraction, whereas a fraction burning above 500 °C appears at 600 °C and becomes the predominant fraction above 650 °C. These trends indicate that the deposition of coke is attenuated, but the deposited coke is more refractory as the reforming temperature increases. Comparing the TPO profiles in Fig. 4a and b, it can be seen that at a reforming temperature of 550 °C the nature of the deposited coke is similar for both values of time on stream, although the coke content increases for the higher time on stream (Fig. 4b). For the reforming temperatures of 650 and 700 °C, the TPO profiles of the coke deposited during the CO_2 capture period (Fig. 4a) and at 300 min reaction time (Fig. 4b) are also similar, especially for the reactions at 700 °C. But interestingly, the TPO profiles of the catalyst samples used at 600 °C in the CO_2 capture period and at the end of the reaction (after saturation of the dolomite) differ significantly, so that the structured coke burning at high temperature is the major coke fraction for the latter sample (used for longer reaction time after dolomite saturation). Moreover, the TPO profiles of the catalyst used at 600, 650 and 700 °C for 300 min in the presence of saturated dolomite (Fig. 4b) differ significantly from those in Fig. S6, corresponding to the SR (without dolomite) of the bio-oil. All these results show a remarkable role of dolomite in coke deposition, with the role of dolomite at a reforming temperature of 600 °C being different from that at higher reforming temperatures.

The results on the nature of the coke (amorphous or filamentous) obtained by TPO analysis have been corroborated by SEM images of the catalyst used at selected operating conditions, shown in Fig. S7. Thus, in the SEM images of the catalyst particles used at 600 °C and with a catalyst/mass ratio of 10 (Figs. S7c and d), a high presence of carbon filaments is observed. Conversely, there are no carbon filaments in the catalyst used at 550 °C with a sorbent/catalyst mass ratio of 10 (Figs. S7a and b), and the presence of carbon filaments is significantly lower than at 600 °C in the catalyst particles used at 700 °C with a sorbent/catalyst mass ratio of 20 (Figs. S7e and f).

Concerning the effect of space time on coke deposition, the comparison of the TPO profiles for two space time values at 600 °C (continuous and dashed red lines in Fig. 4b) confirms the well-known fact that coke deposition in bio-oil reforming is significantly attenuated with decreasing oxygenate concentration (precursors of amorphous coke) [61,64]. In this case, both amorphous and filamentous coke formation are notably attenuated by doubling the space time.

3.2.2. Deterioration of the used catalyst properties

To assess the sintering of Ni crystals and the crystalline state of the

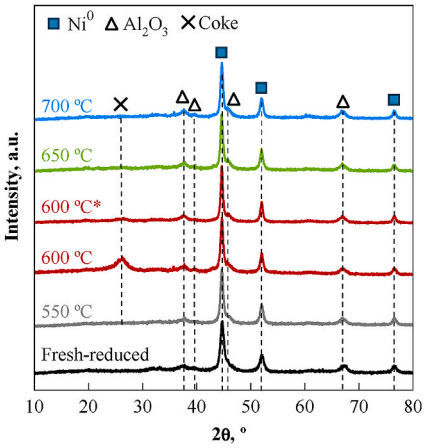

Fig. 5. XRD patterns of fresh-reduced and used catalyst samples in the SESR runs at different temperatures. Reaction conditions: space time, 0.15 $g_{catalyst}$·h/$g_{oxygenates}$ (*0.30 $g_{catalyst}$·h/$g_{oxygenates}$); sorbent/catalyst mass ratio, 10; S/C, 3.4.

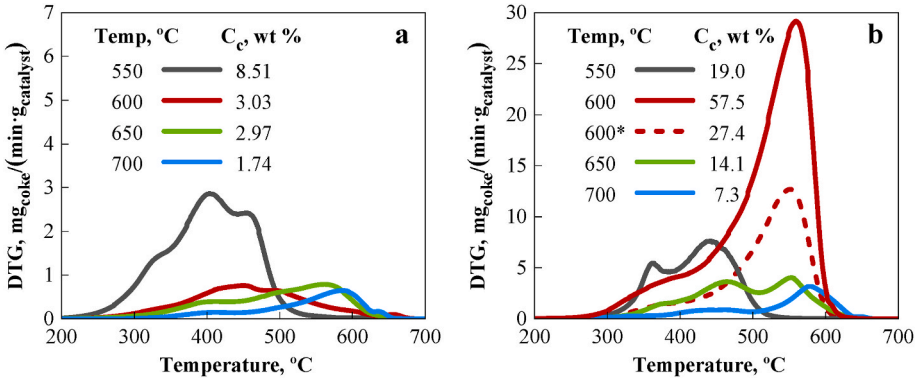

Fig. 4. TPO profiles and coke content (wt%) for the catalyst used at different temperatures in the CO_2 capture period (50 min on stream) (a), and after 300 min on stream (b). Reaction conditions: space time, 0.15 $g_{catalyst}$·h/$g_{oxygenates}$; dolomite/catalyst mass ratio, 10; S/C, 3.4. *space time, 0.30 $g_{catalyst}$·h/$g_{oxygenates}$ for dashed red line in graph b. (For interpretation of the references to color in this figure legend, the reader is referred to the Web version of this article.)

coke deposits, Fig. 5 shows the XRD patterns of the fresh-reduced and used catalyst samples at different temperatures under the conditions of Fig. 1 (sorbent/catalyst mass ratio of 10). XRD results corresponding to a sorbent/catalyst mass ratio of 20 are shown in Fig. S8. Peaks corresponding to Ni^0 (diffraction angle at 44.5° in (111) plane, 51.8° in (200) plane and 75.5° in (110) plane) and Al_2O_3 crystals (37.3°, 45.6° and 66.8°) are identified in the fresh-reduced catalyst. The same diffraction peaks are observed in the catalyst used in the SESR of bio-oil. Similarly, the presence of NiO is not detected, confirming the high reducing capacity of the reaction medium to maintain the active metal in a reduced state. The average size of the Ni crystals of the fresh-reduced and used catalysts (Table 2) was calculated from the diffraction peak at $2\theta = 51.8°$ using the Scherrer equation. The estimated value is 15.0 nm for the fresh-reduced catalyst and increases slightly in the range of 15–20 nm for the used catalyst samples. Based on these results, there is no evidence for a significant sintering phenomenon of Ni crystals.

The XRD patterns of the used catalyst samples also provide information about the coke deposits. The presence of a broad peak at a diffraction angle $2\theta = 26°$ is observed in the catalyst used at 600 °C (more pronounced at the lowest space time). This peak corresponds to high crystallinity coke (graphitic carbon), usually identified in catalysts used in the SR of hydrocarbons [68] and pure oxygenate compounds, such as ethanol and phenol [69], acetone [70], acetic acid [71]. This result is coherent with the TPO profiles in Fig. 4b and the SEM images in Figs. S7c and d, and confirms the structured nature of the main combustion peak in the coke deposited at 600 °C, whose amount decreases significantly with increasing space time. The absence of the diffraction peak at 26° in the coke deposited at 550 °C corroborates its amorphous nature. For the catalysts used in the SESR above 650 °C, although some structured coke is deposited according to the TPO profiles (Fig. 4b), its small amount does not allow it to be detected in the corresponding XRD patterns in Fig. 5.

In order to evaluate the possible deterioration of the porous structure of the catalyst and its contribution to the deactivation, N_2 adsorption-desorption isotherms have been obtained from fresh-reduced and used samples (Fig. S9), from which the physical properties (BET surface area, mean pore diameter and pore volume) have been determined (Table 2). All samples in Fig. S9 show a type IV isotherm, characteristic of mesoporous materials, associated with capillary (pore) condensation taking place in mesopores and the occurrence of multilayer adsorption. The isotherms for fresh-reduced catalyst and samples used at the lower temperature (Fig. S9a) present a hysteresis of the type H2, which is attributed to a difference in mechanism between condensation and evaporation processes occurring in pores with narrow neck and wide bodies. Materials with H2 hysteresis are often disordered and the distribution of pore size and shape is not well defined. Conversely, a H3-type hysteresis cycle is observed in the isotherms of the catalysts used above 600 °C (Figs. S9c,e,g), which shows no limiting adsorption at high P/P_0, and is associated to aggregated plate-like particles that give rise to slit-shaped pores [72].

Overall, there is an evolution of mesoporosity with a slight progressive decrease from the highest temperature to 550 °C. For most of the used samples, the total volume adsorbed at high pressures ($P/P_0 \approx 1$) is lower than that of the fresh-reduced sample, demonstrating the partial blockage of the mesopores, which is more pronounced at the lowest reforming temperature. For all reforming temperatures studied, the BET surface area of the used catalyst decreases with increasing dolomite presence, evidencing a partial blockage of the mesoporous structure of the catalysts, which is promoted at higher sorbent loadings, probably due to the high deposition of a low porosity coke. On the other hand, the increase in BET surface area observed for the used samples at 600 °C (more pronounced at high space time) compared to the fresh-reduced catalyst, suggests that there is an additional porosity created by the filamentous coke deposited on these samples. Overall, the average pore diameter and pore volume decrease compared to the fresh-reduced sample (more noticeable at low temperatures, 550 and 600 °C), probably due to the blockage of part of the porous surface. To sum up, the different BET surface area values (higher or lower than those of the fresh catalyst, depending on the reaction conditions) indicate the formation of both: i) filamentous coke (at 600 °C), which is probably stacked on the surface of the catalyst, causing an increase in the BET surface area, and ii) coke clogging the porous structure, causing a decrease in the BET surface area.

Table 2
Physico-chemical properties (average Ni^0 crystal size (d_{Ni}), BET surface area (S_{BET}), pore volume (V_{pore}) and mean pore diameter (d_{pore}) of fresh-reduced catalyst and used in the SESR of raw bio-oil at different temperatures and sorbent/catalyst mass ratio. Reaction conditions: space time, 0.15 $g_{catalyst}$·h/$g_{oxygenates}$; S/C, 3.4.

Catalyst	Temperature (°C)	d_{Ni} (nm)	S_{BET} (m^2/g)	V_{pore} (cm^3/g)	d_{pore} (nm)
Fresh-reduced	–	15	65.1	0.24	13.1
Used with sorbent/ catalyst mass ratio of 10	550	15	62.3	0.11	7.1
	600	16	69.9	0.18	13.4
	600[a]	20	79.6	0.25	13.4
	650	16	60.6	0.20	14.4
	700	16	65.0	0.26	15.4
Used with sorbent/ catalyst mass ratio of 20	550	16	58.9	0.13	8.3
	600	16	52.1	0.13	10.8
	650	16	55.5	0.16	12.0
	700	17	57.9	0.21	13.1

[a] Space time, 0.30 $g_{catalyst}$·h/$g_{oxygenates}$.

3.3. Cyclic operation with joint regeneration of the catalyst and dolomite

The efficiency of the joint reactivation of catalyst and sorbent has been studied running 7 reaction-regeneration cycles. The conditions in the reaction step (established by the results in section 3.1) are 600 °C, space time of 0.30 $g_{catalyst}$·h/$g_{oxygenates}$ (corresponding to 1 g of catalyst), sorbent/catalyst mass ratio of 10, S/C molar ratio of 3.4, and time on stream of 120 min. These conditions allow to operate with a sufficiently high CO_2 capture time (about 60 min), with the corresponding sorbent/catalyst mass ratio of 10. The regeneration step consisted of coke combustion and CO_2 removal in an external oven at 850 °C for 4 h in air atmosphere (sufficient time for complete removal of coke deposits and CO_2). After each regeneration step, the catalyst + sorbent were subjected to a reduction step (at 850 °C for 4 h in H_2–N_2 (7 vol% H_2)) to obtain the active Ni^0 particles. Fig. 6 shows the evolution with time of the reaction indices in the 1st reaction step (fresh material) (graph a) and in the 7th reaction step (graph b), and Fig. 7 shows the evolution of the H_2 yield in the CO_2 capture period in the successive reaction steps. When comparing the 1st and 7th reaction steps, a rather similar performance of the catalysts/sorbent bed is observed, indicating a good overall recovery in the regeneration step of both solids, the catalyst activity and the CO_2 sorption capacity of the dolomite. Nevertheless, the H_2 yield in the 7th reaction step is slightly lower than that obtained with the fresh catalyst in the 1st reaction, and a small CH_4 yield is observed in the CO_2 capture period.

As observed in Fig. 7, this slight decrease in H_2 yield in the CO_2 capture period occurs in the first two reaction-regeneration cycles, but the catalyst/sorbent bed reaches a stable performance from the 3rd third reaction step onwards. The possible causes of the decrease in H_2 yield in the CO_2 capture period observed in the first two cycles are the incomplete recovery of the CO_2 sorption capacity of the sorbent and/or of the activity for the reforming and WGS reactions of the catalyst. It is interesting to note in Fig. 6 that the duration of the capture period in the 7th reaction step is even slightly longer than in the 1st step, suggesting that the dolomite has fully recovered its CO_2 capture capacity. This result can be observed more clearly in Fig. 8, which shows the evolution over time of the CO_2 yield in different reaction steps (1st, 2nd, 3rd and 7th). As observed, the duration of the CO_2 capture period is shorter in the first cycles and remains constant and longer after the third cycle.

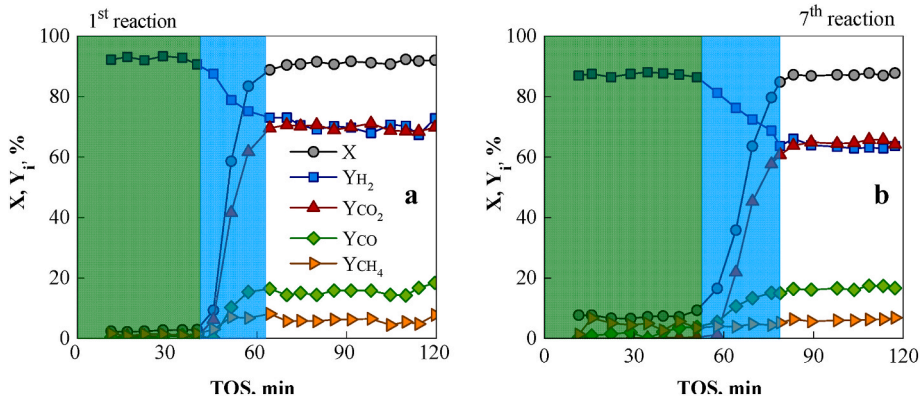

Fig. 6. Evolution with time on stream of carbon conversion and products yields in the 1st (a) and 7th (b) reaction steps (with intermediate regenerations). Reaction conditions: 600 °C; space time, 0.3 $g_{catalyst}$·h/$g_{oxygenates}$; sorbent/catalyst mass ratio, 10; S/C, 3.4. Regeneration conditions: calcination with air in external oven at 850 °C for 4 h. Colored zones: CO_2 capture period (green shade) and breakthrough period (blue shade). (For interpretation of the references to color in this figure legend, the reader is referred to the Web version of this article.)

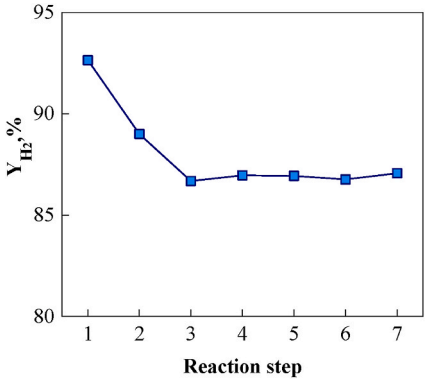

Fig. 7. Evolution of H_2 yield in the CO_2 capture period in successive reaction steps (with intermediate regenerations). Reaction and regeneration conditions of Fig. 6.

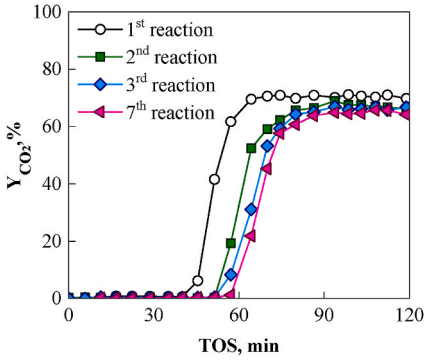

Fig. 8. CO_2 yield evolution with time on stream in successive reaction steps (with intermediate regeneration). Reaction and regeneration conditions of Fig. 6.

Interestingly, the mesoporosity of the dolomite decreases along the reaction-regeneration cycles, as shown by the results in Table S1. The BET surface area and pore volume of the saturated dolomite after the 7th reaction decrease significantly compared to the fresh-calcined dolomite sample, while the mean pore diameter increases, indicating complete sorbent saturation due to CO_2 capture with a selective blockage of the narrower pores. After the regeneration of the dolomite by decarbonation, the mesoporosity is only partially restored, so that the surface area and the mean pore volume are about half of those of the fresh-calcined sample, which shows the partial blockage of the sorbent mesopores after the regeneration period, not being able to fully recover the initial structure of the fresh-calcined dolomite. Nevertheless, the dolomite retains its CO_2 capture capacity. Consequently, the decrease in H_2 yield during the CO_2 capture period in the first cycles (Fig. 7) should be attributed to the irreversible deactivation of the catalyst in the first two reaction-regeneration cycles and not to the deterioration of the CO_2 capture capacity of the dolomite, as studied in section 3.4.

3.4. Characterization of catalyst used in the cyclic operation

The catalyst used in some reaction steps, and also the catalyst regenerated after the 7th reaction, have been characterized by several techniques (TPO, TPR, XRD, N_2 adsorption-desorption and XPS) (section 2.2) in order to analyze the possible changes in the physico-chemical properties of the catalyst along the cyclic operation and to correlate them with the kinetic performance observed in section 3.3.

3.4.1. Coke deposition

Fig. 9 depicts the TPO profiles of the catalyst used after the 1st and 7th reaction steps. For both samples, there is a major combustion peak burning above 500 °C corresponding to filamentous and structured coke, with a low amount of amorphous coke burning below 500 °C. The coke content decreases in the successive reaction steps (from 17.2 wt% in the first reaction to 12.8 wt% in the seventh reaction), especially the filamentous coke, whereas the amorphous carbon remains fairly constant. The difference in coke deposition in Fig. 9 is consistent with the slightly lower catalyst activity observed after the first two reaction-regeneration

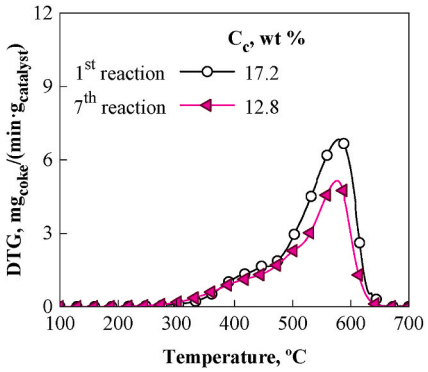

Fig. 9. Comparison of the TPO profiles and coke content (wt%) deposited on samples used in the 1st and 7th reaction steps. Reaction and regeneration conditions of Fig. 6.

cycles (Fig. 7).

3.4.2. Deterioration of the catalyst properties

Fig. 10 shows the TPR profiles of the fresh catalyst and the catalyst regenerated after the 7th reaction step. Both samples require a high temperature for the complete reduction of all the Ni species, consistent with the predominant presence of the $NiAl_2O_4$ spinel structure in the fresh and regenerated catalysts. The TPR profile of the fresh catalyst shows a broad and asymmetric reduction peak between 500 and 900 °C, with its maximum at 750 °C. The regenerated catalyst has a similar TPR profile to the fresh catalyst, but shows a more symmetrical and slightly less wide reduction peak, which suggests that the reconstructed $NiAl_2O_4$ spinel is more homogeneous. Besides, the maximum is shifted to a higher reduction temperature (peak at 775 °C), indicating that a higher temperature is required for the complete reduction of the reconstructed Ni spinel structure in the regenerated catalyst. Moreover, a small content of NiO species is also observed in the 300–500 °C range of this sample, which means that the spinel is not fully restored after successive reaction-regeneration steps.

The Ni content of the regenerated catalyst after the 7th reaction step was quantified by H_2-TPR treatment carried out in a thermobalance (up to 1000 °C to ensure complete reduction of Ni) by determining the mass loss associated with the H_2O formed. The calculated Ni content (29.1 wt %) is practically the same as that determined for the fresh catalyst (30.7 wt%), showing that there is no significant loss of Ni in the successive reaction-regeneration cycles. XPS analysis (Table 3) was also used to quantify the changes in surface Ni content on the fresh and reconstructed spinel after the reaction-regeneration cycles. It is noteworthy that the surface Ni content of the fresh spinel is slightly lower than its average Ni content, indicating that the Ni crystals are not completely uniformly distributed on the catalyst particle after spinel reduction, with the content of internal Ni being slightly higher than that in the surface of the particle. Moreover, the external Ni content decreases slightly after the first two reaction-regeneration cycles and then remains almost constant in the subsequent reaction steps. This result suggests that there is a slight redistribution of Ni towards the interior of the catalyst particles after the first two reaction-regeneration cycles, but a stable and fully reproducible redispersion of the Ni crystals is achieved in the subsequent cycles.

The XRD diffractograms of the used catalyst samples after the 1st and 7th reaction steps are plotted in Fig. 11, together with the XRD diffractogram of the fresh-reduced catalyst for comparison. Similar to the samples used at 600 °C in 300 min runs (Fig. 5), the species identified in the XRD pattern of the catalyst used after the 1st reaction step are Ni^0, Al_2O_3 and some crystalline coke. The decrease in the intensity of the crystalline coke in the XRD diffractograms of the spent catalyst used in the 7th reaction compared to that of the 1st reaction is consistent with the decrease in the fraction of filamentous coke in Fig. 9. However, the XRD pattern of the sample corresponding to the 7th reaction step (blue line in Fig. 11) shows that some $NiAl_2O_4$ spinel species still remain in the spent sample. This result proves that the spinel structure (reconstructed in the regeneration step, as shown by the green curve in Fig. 11) is not completely reduced at the reduction temperature used in the reaction-regeneration cycles (850 °C). However, after reduction of the regenerated catalyst at 900 °C (externally, in a Micromeritics AutoChem II 2920 apparatus), the only species observed are Ni^0 and Al_2O_3 (red curve in Fig. 11), as in the fresh-reduced (at 850 °C) catalyst. This result is in agreement with the TPR results (Fig. 10) and shows that a higher reduction temperature (>850 °C) is required for the complete reduction of the $NiAl_2O_4$ spinel after the joint regeneration of the catalyst/sorbent bed. It should be noted that the Ni^0 crystal size (calculated by the Scherrer equation from the diffraction peak at $2\theta = 51.8°$ (plane (200)) for the catalyst used in the 7th reaction step (14 nm) is even slightly smaller than for the fresh-reduced catalyst (15 nm), confirming that there is no sintering of the Ni^0 crystals under the conditions studied.

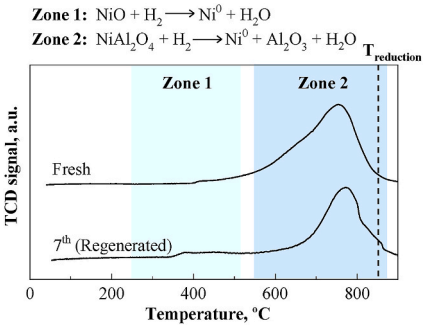

Fig. 10. TPR profiles of fresh catalyst and regenerated after the 7th reaction step. Reaction and regeneration conditions of Fig. 6.

Table 3
Surface Ni content evolution on the fresh and reconstructed spinel after successive reaction-regeneration cycles determined by XPS analysis.

Cycle	Ni, wt%
Fresh $NiAl_2O_4$ spinel	22.8
1st reaction-regeneration	20.8
3rd reaction-regeneration	17.9
7th reaction-regeneration	18.6

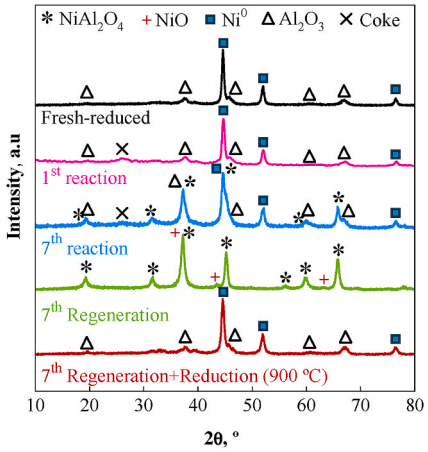

Fig. 11. XRD patterns of the fresh-reduced catalyst, the catalyst used in the 1st and 7th reaction steps, the catalyst regenerated after the 7th step, and after its subsequent reduction at 900 °C. Reaction and regeneration conditions of Fig. 6.

4. Discussion

4.1. On the effect of reaction conditions on the sorbent/catalyst performance

The results in Fig. 2 show that the reforming temperature and the dolomite/catalyst mass ratio have a significant effect on the yield of products in the SESR de raw bio-oil. The best compromise between the reaction temperature and the value of the sorbent/catalyst mass ratio, in order to maximize the yield and purity of H_2, corresponds to intermediate values of both variables: 600–650 °C and a sorbent/catalyst mass ratio of 10. This result is explained by the different impact of these parameters on the reactions occurring on the two solids present in the catalytic bed (Eqs. (1)–(11)). At lower temperatures, the rate of the reforming and WGS reactions over the catalyst is limited, favoring the decomposition/cracking reactions of oxygenates (Eq. (4)) over dolomite (especially at high dolomite/catalyst ratios), thus leading to lower H_2 yield and higher formation of CH_4 as a by-product. At temperatures

above 650 °C, the high H_2 yield is offset by its dilution with CO_2 and CO, due to the lower adsorption capacity of dolomite and the formation of CO favored by the reverse-WGS reaction (reverse of Eq. (2)), with little effect of the dolomite/catalyst ratio on the product distribution in the CO_2 capture period at these high temperatures.

The evolution of the product distribution with time on stream in the post-breakthrough period (after CO_2 capture) in Figs. 1 and 3 and S5 is a consequence of the catalyst deactivation, whose main cause is the coke deposition, since the XRD analysis (Table 2) for the catalyst samples used under different conditions does not show significant differences in the Ni^0 crystal size, which allows ruling out Ni sintering as a deactivation cause for this catalyst under SESR conditions, similarly to that observed previously under SR conditions [61]. Consequently, the different effects of the operating conditions on the observed deactivation rate should be explained by the differences in the deposition rate and the nature of the coke. Thus, at a reforming temperature of 550 °C, there is a rapid deposition of amorphous coke during the CO_2 capture period (Fig. 4a), which is deposited on the metal sites and clogs the porous structure, thus decreasing the BET surface area (Table 2). Based on studies of coke deposition on Ni catalysts in SR [63,64] and SESR [53,57] of bio-oil, the main origin of this amorphous coke is the decomposition/cracking of oxygenates (Eq. (4)). The partial blockage of the mesopores is coherent with the rapid deactivation observed at this low temperature. The deposition of the same type of amorphous coke continues for the rest of the reaction at 550 °C (Fig. 4b), although more slowly than during the CO_2 capture period. Moreover, it is noteworthy that the content of amorphous coke in Fig. 4a decreases with increasing temperature, as its gasification is promoted (Eq. (10)), whereas the formation of coke burning above 500 °C is favored, which can be related to both the filamentous coke formed by CH_4 decomposition (Eq. (8)) and the Boudouard reaction (Eq. (9)) [73] or to the decomposition/cracking of oxygenates (Eq. (4)) [58].

The differences between the TPO profiles of the catalyst samples used in the SESR runs with a dolomite/catalyst ratio of 10 for 300 min (Fig. 4b) and those of the samples used in the SR reactions and the same reforming temperature (Fig. S6, without dolomite) prove the relevant role of dolomite on the nature and amount of coke deposited over the Ni-based catalyst, with this role being different at 600 °C than at higher reforming temperature. Thus, at 600 °C, a moderate presence of dolomite favors the deposition of structured coke of filamentous nature, as revealed by the high combustion peak burning at high temperature and also demonstrated by SEM images (Figs. S7c and d). The increase in the BET surface area of the samples used at 600 °C with respect to the fresh-reduced catalyst (Table 2) is also coherent with the presence of porous carbon structures, such as carbon filaments. In our previous work [57], this higher deposition of filamentous coke in the SESR at 600 °C was explained by the synergy of the coke formation mechanism on the catalyst and the dolomite. This synergy is facilitated by the good contact between the two solids in the fluidized-bed reactor, which increases the formation of filamentous coke structures. However, this role of dolomite in promoting filamentous coke deposition is not relevant at 650 and 700 °C because at these temperatures the coke formation mechanisms are limited by gasification and, furthermore, the formation of filamentous coke by the Boudouard reaction is disfavored with increasing temperature. The attenuation of coke deposition on Ni-based catalysts above 700 °C and a S/C ratio above 2 has been tested in the literature on the SR of biomass gasification gas [74]. Conversely, the presence of dolomite at high reforming temperature attenuates the deposition of structured coke, as evidenced by the small combustion peak burning at high temperature in the TPO profiles of Fig. 4b compared to those observed in Fig. S6 corresponding to SR conditions, and the low amount of filamentous coke observed in the SEM images of the samples used in the SESR reactions at 700 °C (Fig. S7e f). This result can be explained by the contribution of dolomite to the reforming of oxygenates from bio-oil at high temperatures [60], which is evidenced when comparing the results in Fig. 1a (SESR) and Fig. S4a (SR). Besides, the activity of dolomite for tar gasification is well established [75,76], so it is likely to be active in the gasification of coke evolution intermediates. Consequently, the stability at 700 °C is higher in the SESR runs with a dolomite/sorbent ratio of 10 than in the SR runs (compare blue markers in Fig. 1 and S4).

Nevertheless, the use of a high sorbent/catalyst mass ratio (of 20 in this study), although increases the CO_2 capture time (compare Fig. 1 and S5), has the disadvantage of a lower stability of the Ni catalyst, since it favors the formation of amorphous coke by decomposition/cracking of oxygenates (Eq. (4)) activated by the dolomite. This higher deposition of amorphous coke causes a higher blockage of the mesoporous structure, as evidenced by the higher decrease in BET surface area (Table 2) for the samples, and explains the faster deactivation rate for the higher dolomite/catalyst ratio.

Regarding the effect of space time, the higher catalyst stability observed in Fig. 3 compared to Fig. 1 (red markers) can also be explained by the significant reduction in the deposition of both amorphous and filamentous coke (compare red curves in Fig. 4b).

4.2. On the results of the operation in reaction-regeneration cycles

The scale-up of SESR of bio-oil requires the operation in reaction-regeneration cycles, recovering the CO_2 capture capacity of the sorbent (by decarbonation) and reactivating the catalyst (by coke combustion). The challenge is to perform these operations simultaneously and in the same unit, avoiding the technological difficulties of separating and treating the two materials. The $NiAl_2O_4$ spinel-derived catalyst is particularly attractive for this purpose because the spinel is completely reconstructed by coke combustion at a high temperature (850 °C, which is necessary for the efficient decarbonation of dolomite) and the subsequent reduction at 850 °C of the reconstructed $NiAl_2O_4$ spinel achieves a good dispersion of Ni crystals on the Al_2O_3 support, recovering the activity of the fresh Ni/Al_2O_3, without the sintering problems of supported Ni catalysts prepared by impregnation [56,77]. Dang et al. [78] highlight the regenerability of Ni/Al_2O_3 derived from $NiAl_2O_4$ spinel in the dry reforming of CH_4, explaining the reversible phase change of this catalyst (between $NiAl_2O_4$ and Ni/Al_2O_3) in successive oxidation (coke combustion)/reduction treatments. These authors propose a strategy of surface spatial confinement in γ-Al_2O_3 layers to mitigate the sintering by migration of Ni under high temperature regeneration conditions (required for high amounts of coke).

The results presented in section 3.3 (Figs. 6 and 7) have shown that the behavior of the system composed of Ni/Al_2O_3 catalyst derived from $NiAl_2O_4$ spinel and dolomite in the SESR of bio-oil in successive reaction-regeneration cycles is quite satisfactory, as it allows a reproducible performance from the 3rd reaction cycle onwards. It should be noted that this trend towards a stabilization operating in reaction-regeneration cycles has also been observed in a commercial Ni supported on Ca–Al_2O_3 catalyst used in the on-line SR of pyrolysis volatiles from biomass [79] and high-density polyethylene (HDPE) [80]. However, the remaining activity in the pseudo-stable state is higher in the catalyst used in the present work, which is explained by the aforementioned regeneration capacity of the $NiAl_2O_4$ spinel.

The small loss of catalyst activity observed between the first two reaction-regeneration cycles is not due to the deterioration of the CO_2 capture capacity of the dolomite, as revealed by the fact that the duration of the CO_2 capture period in the 7th reaction step is even slightly longer (about 50 min) than in the 1st reaction step (about 40 min). Consequently, the loss of activity can be attributed to the deterioration of the catalyst properties in the first reaction steps, although the catalyst reaches an apparent stabilization (constant H_2 yield, Fig. 7) after two reaction-regeneration cycles. This slight irreversible deactivation of the catalyst is a consequence of the loss of active Ni species on the catalyst surface due to the incomplete reduction of the regenerated spinel at the reduction temperature used (850 °C), as revealed by the presence of some $NiAl_2O_4$ spinel species in the XRD analysis of the catalyst used in the 7th reaction step (Fig. 11). Moreover, the results in Fig. 8 evidence

that subjecting the dolomite jointly with the catalyst to the successive reduction steps, prior to each reaction, does not have a negative impact on the performance of the dolomite.

4.3. Relevance of the results for scale-up

The results of section 3.1 show that, with the right catalyst and conditions, SESR from raw bio-oil is an attractive route for the production of high purity H_2 from biomass, while minimizing CO_2 emissions, in the transition period towards the universal use of green H_2 produced by H_2O electrolysis.

Table 4 lists some results and reaction conditions from previous literature on the SESR of pure oxygenates (model bio-oil compounds), aqueous fraction of bio-oil, simulated bio-oil and raw bio-oils of different origin, including the results of this work at the end. The raw bio-oil is a complex mixture of oxygenates (Table 1) with different individual reactivity in the reforming [48], which does not allow a direct comparison of the results with those corresponding to pure oxygenates. However, the comparison with the results of other works that have used raw bio-oils shows the good performance of the catalyst used in this work (derived from the reduction of $NiAl_2O_4$ spinel) for the reforming of this complex feed, allowing to obtain higher H_2 yields with a more moderate operating temperature than in previous works, which ratifies its interest for this process.

The interest of SESR scale-up of raw bio-oil is also justified by its integration with biomass fast pyrolysis, which has had a remarkable technological development [82], incorporating as feeds agricultural waste [83] and microalgae [84], and with reactors that facilitate scale-up [85]. From the perspective of scale-up, the use of a bubbling fluidized-bed reactor in the experiment of this work is interesting to extrapolate the results, in particular for the design of a bubbling fluidized-bed reactor with catalyst and sorbent circulation, with the conditions and residence time of both suitable to maintain the complete capture of CO_2 (conditions established in section 3.1). In this reaction-regeneration system, which is also used in various catalytic processes subject to rapid catalyst deactivation, the catalyst is regenerated in another unit and continuously recycled to the reactor to keep the capacity of the catalyst/sorbent system constant [86]. In addition, as noted in a thermodynamic study [87], SESR of raw bio-oil not only has a lower energy requirement than the SR process, but can also provide good performance in the autothermal regime.

The study has been carried out in this work using dolomite as sorbent, whose low cost would facilitate its use on a larger scale. Moreover, as studied in section 3.1, it has a high CO_2 adsorption capacity and does not play a negative role on the catalyst performance (except for a high sorbent/catalyst ratio, for which it favors the formation of amorphous coke that deactivates the catalyst). Joint regeneration of catalyst and sorbent is a strategy that facilitates large-scale operation. As shown in section 3.4, by performing this simple operation (coke combustion with air) under the right conditions (850 °C and 4 h), the $NiAl_2O_4$ spinel is reconstructed, which allows the Ni/Al_2O_3 catalyst to be reactivated after further reduction of the spinel. It has also been shown that although the catalyst reaches a pseudo-stable state of constant activity after the first 3 cycles of reaction-regeneration at 850 °C, the reduction at 900 °C facilitates the complete reduction of Ni and minimizes the irreversible deactivation in these first cycles. It is relevant that dolomite shows a deterioration of physical properties (specific surface area and pore volume) after its successive regenerations, but nevertheless it maintains the sorption capacity. The disadvantage of its limited mechanical strength would require the replacement of a used dolomite purge with fresh dolomite.

5. Conclusions

The results obtained in this work are interesting to integrate two processes, such as fast pyrolysis and SESR of raw bio-oil product, to produce high purity H_2 from lignocellulosic or other biomass (such as microalgae), while minimizing CO_2 emission. Using a Ni/Al_2O_3 catalyst derived from $NiAl_2O_4$ spinel and dolomite as CO_2 sorbent, the temperature range of 600–650 °C and a sorbent/catalyst mass ratio of 10 are suitable conditions to maximize the yield (~92 %) and purity (~99 %) of H_2 in the capture period during SESR of bio-oil with limited catalyst and sorbent deactivation, thus improving the results compared to SR and avoiding CO_2 emissions. The H_2 yield is significantly lower at 550 °C (75 %) because the reforming activity of the catalyst is reduced (especially for CH_4 reforming), while at 700 °C the H_2 selectivity is lower (94 %) because the CO_2 capture capacity of the dolomite is disfavored. Doubling the space time (from 0.15 $g_{catalyst}·h/g_{oxygenates}$ to 0.30 $g_{catalyst}·h/g_{oxygenates}$), while maintaining the dolomite/catalyst ratio of 10, allows the duration of the effective CO_2 capture period to be increased from about 30 min to about 50 min, with higher catalyst stability.

Table 4
Background of H_2 production by SESR from different oxygenated feeds.

Feeding	Reactor	Operating conditions	Catalyst and sorbent	H_2 yield	Ref.
Simulated Bio-oil/ Biogas blend	Fluidized bed	625 °C; S/C = 5.3; P = 2.5 bar WHSV = 1.3 h^{-1} sorbent/catalyst ratio = 20	Pd/Ni–Co HT Artic dolomite	87.1 % (purity 98.6 %)	[81]
Acetic acid/ acetone blends	Fluidized bed	475-675 °C; S/C = 3.7; WHSV = 0.51–0.71 h^{-1} sorbent/ catalyst ratio = 5	Pd/Ni–Co HT Artic dolomite	83.3–88.6 % at 575 °C (purity 99.2–99.4 %)	[32]
Acetic acid	Packed bed	575 °C; S/C = 5; WHSV = 0.8 h^{-1} sorbent/catalyst ratio = 5	Ni, NiCo and NiCoPd supported on Al_2O_3 or olivine, Ni/HTC	~90 % (Al_2O_3 supported catalysts) and 60–80 % (olivine supported catalysts) for the simulated bio-oil with artic dolomite	[43]
Simulated bio-oil		575 °C; S/C = 7; WHSV = 3.8 h^{-1} sorbent/catalyst ratio = 5	Artic/Castro dolomite		
Bio-oil aqueous fraction	Packed bed	500-700 °C water/bio-oil ratio = 1–4 Sorbent loading = 11 g	Commercial Ni-based catalyst (Z417) Dolomite	75 % (600 °C and water/bio –oil ratio = 1)	[49]
Bio-oil aqueous fraction	Fluidized bed	550-650 °C; S/C = 10 space time = 0.45–1.35 $g_{cat}·h/g_{bio-oil}$ sorbent/catalyst ratio = 2.6–33.3	$Ni/La_2O_3–α-Al_2O_3$ Dolomite	~99 % (600 °C, dolomite/catalyst/≤ 5.9 and 0.45 $g_{cat}·h/g_{bio-oil}$)	[50]
Bio-oil (corn cob)	Packed bed	650-850 °C; S/C = 9-15 L_SHSV = 0.08–0.23 h^{-1} CaO/(Carbon in bio-oil) = 3	$Ni–Ce/Co/Al_2O_3$ CaO	85 % (750–800 °C, S/C = 12 and L_SHSV = 0.15 h^{-1})	[51]
Bio-oil (poplar sawdust)	Packed bed	550 °C; S/C = 4, LHSV = 0.48 mL/ g·h Ce/Ca ratio = 0, 0.04, 0.2, 0.24, 0.3	$Ni/Ce_xZr_1Ca_5$	~78 % with Ce/Ca = 0.24 (purity >90 %)	[35]
Bio-oil (pine sawdust)	Fluidized bed	550 -700 °C; S/C = 3.4 space time = 0.15–0.30 $g_{cat}·h/g_{bio-oil}$	Ni/Al_2O_3 derived from $NiAl_2O_4$ Dolomite	>92 % (600–650 °C, sorbent/catalyst = 10)	This work

The catalyst/sorbent system studied is interesting for the scale-up of bio-oil SESR due to its good performance in reaction-regeneration cycles. Thus, the joint regeneration of the two materials is possible with a treatment at 850 °C in air for 4 h. Under these conditions and with the subsequent reduction at 850 °C, the catalyst undergoes a partial irreversible deactivation in the first two cycles, after which it reaches a pseudo-stable state in which it completely recovers its activity in the subsequent reaction-regeneration cycles. This irreversible deactivation can be minimized by increasing the reduction temperature of the spinel to 900 °C.

Declaration of competing interest

The authors declare that they have no known competing financial interests or personal relationships that could have appeared to influence the work reported in this paper.

Acknowledgements

This work has been carried out with the financial support of the grant PID2021-127005OB-I00 funded by MCIN/AEI/10.13039/501100011033 and by "ERDF A way of making Europe", the European Commission (HORIZON H2020-MSCA RISE 2018. Contract No. 823745) and the Department of Education, Universities and Investigation of Basque Government (Project IT1645-22 and PhD grant PRE_2022_2_0141 for L. Landa). The authors thank for technical and human support provided by SGIker (UPV/EHU), and to Calcinor S.A. for supplying the dolomite.

Appendix A. Supplementary data

Supplementary data to this article can be found online at https://doi.org/10.1016/j.ijhydene.2024.01.228.

References

[1] Capurso T, Stefanizzi M, Torresi M, Camporeale SM. Perspective of the role of hydrogen in the 21st century energy transition. Energy Convers Manag 2022;114898:251. https://doi.org/10.1016/j.enconman.2021.114898.

[2] Cordero-Lanzac T, Ramirez A, Navajas A, Gevers L, Brunialti S, Gandía LM, et al. A techno-economic and life cycle assessment for the production of green methanol from CO_2: catalyst and process bottlenecks. J Energy Chem 2022;68:255–66. https://doi.org/10.1016/j.jechem.2021.09.045.

[3] Ateka A, Rodriguez-Vega P, Ereña J, Aguayo AT, Bilbao J. A review on the valorization of CO_2. Focusing on the thermodynamics and catalyst design studies of the direct synthesis of dimethyl ether. Fuel Process Technol 2022;107310:233. https://doi.org/10.1016/j.fuproc.2022.107310.

[4] Liu L, Zhai R, Hu Y. Performance evaluation of wind-solar-hydrogen system for renewable energy generation and green hydrogen generation and storage: energy, exergy, economic, and enviroeconomic. Energy 2023;127386:276. https://doi.org/10.1016/j.energy.2023.127386.

[5] Vishwakarma AK, Hussain M, Verma SK, Shukla V, Shaz MA, Srivastava ON. Synthesis and characterizations of graphene/Sm doped $BiFeO_3$ composites photoanode for efficient photo-electrochemical water splitting. Int J Hydrogen Energy 2021;46:15550–60. https://doi.org/10.1016/j.ijhydene.2021.02.115.

[6] Rezayeenik M, Mousavi-Kamazani M, Zinatloo-Ajabshir S. $CeVO_4$/rGO nanocomposite: facile hydrothermal synthesis, characterization, and electrochemical hydrogen storage. Appl Phys Mater Sci Process 2023;129:1–12. https://doi.org/10.1007/s00339-022-06325-y/metrics.

[7] Esfahani MH, Zinatloo-Ajabshir S, Naji H, Marjerrison CA, Greedan JE, Behzad M. Structural characterization, phase analysis and electrochemical hydrogen storage studies on new pyrochlore $SmRETi_2O_7$ (RE = Dy, Ho, and Yb) microstructures. Ceram Int 2023;49:253–63. https://doi.org/10.1016/j.ceramint.2022.08.338.

[8] Zonarsaghar A, Mousavi-Kamazani M, Zinatloo-Ajabshir S. Sonochemical synthesis of $CeVO_4$ nanoparticles for electrochemical hydrogen storage. Int J Hydrogen Energy 2022;47:5403–17. https://doi.org/10.1016/j.ijhydene.2021.11.183.

[9] Zinatloo-Ajabshir S, Morassaei MS, Amiri O, Salavati-Niasari M, Foong LK. $Nd_2Sn_2O_7$ nanostructures: green synthesis and characterization using date palm extract, a potential electrochemical hydrogen storage material. Ceram Int 2020;46:17186–96. https://doi.org/10.1016/j.ceramint.2020.03.014.

[10] Zinatloo-Ajabshir S, Salehi Z, Amiri O, Salavati-Niasari M. Green synthesis, characterization and investigation of the electrochemical hydrogen storage properties of $Dy_2Ce_2O_7$ nanostructures with fig extract. Int J Hydrogen Energy 2019;44:20110–20. https://doi.org/10.1016/j.ijhydene.2019.05.137.

[11] Martinez-Burgos WJ, de Souza Candeo E, Pedroni Medeiros AB, Cesar de Carvalho J, Oliveira de Andrade Tanobe V, Soccol CR, et al. Hydrogen: current advances and patented technologies of its renewable production. J Clean Prod 2021;124970:286. https://doi.org/10.1016/j.jclepro.2020.124970.

[12] Ghodke PK, Sharma AK, Jayaseelan A, Gopinath KP. Hydrogen-rich syngas production from the lignocellulosic biomass by catalytic gasification: a state of art review on advance technologies, economic challenges, and future prospectus. Fuel 2023;127800:342. https://doi.org/10.1016/j.fuel.2023.127800.

[13] AlHumaidan FS, Absi Halabi M, Rana MS, Vinoba M. Blue hydrogen: current status and future technologies. Energy Convers Manag 2023;116840:283. https://doi.org/10.1016/j.enconman.2023.116840.

[14] Wu H, Alkhatami AG, Farhan ZA, AbdalSalam AG, Hamadan R, Aldarrji MQ, et al. Recent developments in the production of hydrogen: efficiency comparison of different techniques, economic dimensions, challenges and environmental impacts. Fuel Process Technol 2023;107819:248. https://doi.org/10.1016/j.fuproc.2023.107819.

[15] Kong G, Zhang X, Wang K, Li J, Zhou L, Wang J, et al. Coupling biomass gasification and inline co-steam reforming: synergistic effect on promotion of hydrogen production and tar removal. Fuel Process Technol 2023;107689:243. https://doi.org/10.1016/j.fuproc.2023.107689.

[16] Arregi A, Amutio M, Lopez G, Bilbao J, Olazar M. Evaluation of thermochemical routes for hydrogen production from biomass: a review. Energy Convers Manag 2018;165:696–719. https://doi.org/10.1016/j.enconman.2018.03.089.

[17] Lepage T, Kammoun M, Schmetz Q, Richel A. Biomass-to-hydrogen: a review of main routes production, processes evaluation and techno-economical assessment. Biomass Bioenergy 2021;105920:144. https://doi.org/10.1016/j.biombioe.2020.105920.

[18] Nikolaidis P, Poullikkas A. A comparative overview of hydrogen production processes. Renew Sustain Energy Rev 2017;67:597–611. https://doi.org/10.1016/j.rser.2016.09.044.

[19] Pafili A, Charisiou ND, Douvartzides SL, Siakavelas GI, Wang W, Liu G, et al. Recent progress in the steam reforming of bio-oil for hydrogen production: a review of operating parameters, catalytic systems and technological innovations. Catalysts 2021;1526:11. https://doi.org/10.3390/catal11121526.

[20] Lee D, Nam H, Won Seo M, Hoon Lee S, Tokmurzin D, Wang S, et al. Recent progress in the catalytic thermochemical conversion process of biomass for biofuels. Chem Eng J 2022;137501:447. https://doi.org/10.1016/j.cej.2022.137501.

[21] Valle B, Remiro A, García-Gómez N, Gayubo AG, Bilbao J. Recent research progress on bio-oil conversion into bio-fuels and raw chemicals: a review. J Chem Technol Biotechnol 2019;94:670–89. https://doi.org/10.1002/jctb.5758.

[22] Elkasabi Y, Jones K, Mullen CA, Strahan GD, Wyatt VT. Spinning band distillation of biomass pyrolysis oil phenolics to produce pure phenol. Sep Purif Technol 2023;123603:314. https://doi.org/10.1016/j.seppur.2023.123603.

[23] Dou B, Wang C, Song Y, Chen H, Jiang B, Yang M, et al. Solid sorbents for in-situ CO_2 removal during sorption-enhanced steam reforming process: a review. Renew Sustain Energy Rev 2016;53:536–46. https://doi.org/10.1016/j.rser.2015.08.068.

[24] Harrison DP. Sorption-enhanced hydrogen production: a review. Ind Eng Chem Res 2008;47:6486–501. https://doi.org/10.1021/ie800298z.

[25] Shokrollahi Yancheshmeh M, Radfarnia HR, Iliuta MC. High temperature CO_2 sorbents and their application for hydrogen production by sorption enhanced steam reforming process. Chem Eng J 2016;283:420–44. https://doi.org/10.1016/j.cej.2015.06.060.

[26] Yan Y, Manovic V, Anthony EJ, Clough PT. Techno-economic analysis of low-carbon hydrogen production by sorption enhanced steam methane reforming (SE-SMR) processes. Energy Convers Manag 2020;113530:226. https://doi.org/10.1016/j.enconman.2020.113530.

[27] Yan Y, Thanganadar D, Clough PT, Mukherjee S, Patchigolla K, Manovic V, et al. Process simulations of blue hydrogen production by upgraded sorption enhanced steam methane reforming (SE-SMR) processes. Energy Convers Manag 2020;113144:222. https://doi.org/10.1016/j.enconman.2020.113144.

[28] Udemu C, Font-Palma C. Modelling of sorption-enhanced steam reforming (SE-SR) process in fluidised bed reactors for low-carbon hydrogen production: a review. Fuel 2023;127588:340. https://doi.org/10.1016/j.fuel.2023.127588.

[29] Di Giuliano A, Gallucci K. Sorption enhanced steam methane reforming based on nickel and calcium looping: a review. Chem Eng Process - Process Intensif 2018;130:240–52. https://doi.org/10.1016/j.cep.2018.06.021.

[30] Di Nardo A, Savuto E, Calchetti G, Stendardo S. Computational particle fluid dynamics 3D simulation of the sorption-enhanced steam methane reforming process in a dual fluidized bed of bifunctional sorbent-catalyst particles. Powder Technol 2023;118568:424. https://doi.org/10.1016/j.powtec.2023.118568.

[31] Gil MV, Fermoso J, Pevida C, Chen D, Rubiera F. Production of fuel-cell grade H_2 by sorption enhanced steam reforming of acetic acid as a model compound of biomass-derived bio-oil. Appl Catal B Environ 2016;184:64–76. https://doi.org/10.1016/j.apcatb.2015.11.028.

[32] Esteban-Díez G, Gil MV, Pevida C, Chen D, Rubiera F. Effect of operating conditions on the sorption enhanced steam reforming of blends of acetic acid and acetone as bio-oil model compounds. Appl Energy 2016;177:579–90. https://doi.org/10.1016/j.apenergy.2016.05.149.

[33] Zhao X, Xue Y, Yan C, Wang Z, Guo C, Huang S. Sorbent assisted catalyst of Ni-CaO-La_2O_3 for sorption enhanced steam reforming of bio-oil with acetic acid as the model compound. Chem Eng Process - Process Intensif 2017;119:106–12. https://doi.org/10.1016/j.cep.2017.05.012.

[34] Omoniyi OA, Dupont V. Optimised cycling stability of sorption enhanced chemical looping steam reforming of acetic acid in a packed bed reactor. Appl Catal B Environ 2019;242:397–409. https://doi.org/10.1016/j.apcatb.2018.09.083.

[35] Li D, Xue H, Hu R. Effect of Ce/Ca ratio in Ni/CeO_2-ZrO_2-CaO catalysts on high-purity hydrogen production by sorption-enhanced steam reforming of acetic acid and bio-oil. Ind Eng Chem Res 2020;59:1446–56. https://doi.org/10.1021/acs.iecr.9b04758.

[36] Oliveira CC, Hori CE. Hydrogen production from sorption enhanced steam reforming of ethanol using bifunctional Ni and Ca-based catalysts doped with Mg and Al. Int J Hydrogen Energy 2023. https://doi.org/10.1016/j.ijhydene.2023.04.178.

[37] Wang S, Xu S, Liu S, Hu B. Prediction of sorption-enhanced reforming process on hydrotalcite sorbent in a fluidized bed reactor. Energy Convers Manag 2019;180:924–30. https://doi.org/10.1016/j.enconman.2018.11.005.

[38] Dang C, Wu S, Yang G, Cao Y, Wang H, Peng F, et al. Hydrogen production from sorption-enhanced steam reforming of phenol over a Ni-Ca-Al-O bifunctional catalyst. ACS Sustainable Chem Eng 2020;8:7111–20. https://doi.org/10.1021/acssuschemeng.0c01267.

[39] Wang X, He Y, Xu T, Xiao B, Liu S, Hu Z, et al. CO_2 sorption-enhanced steam reforming of phenol using Ni–M/CaO–$Ca_{12}Al_{14}O_{33}$ (M = Cu, Co, and Ce) as catalytic sorbents. Chem Eng J 2020;124769:393. https://doi.org/10.1016/j.cej.2020.124769.

[40] Sánchez N, Encinar JM, González JF. Sorption enhanced steam reforming of glycerol: use of La-modified Ni/Al_2O_3 as catalyst. Ind Eng Chem Res 2016;55:3736–41. https://doi.org/10.1021/acs.iecr.5b04084.

[41] Dang C, Yu H, Wang H, Peng F, Yang Y. A bi-functional Co–CaO–$Ca_{12}Al_{14}O_{33}$ catalyst for sorption-enhanced steam reforming of glycerol to high-purity hydrogen. Chem Eng J 2016;286:329–38. https://doi.org/10.1016/j.cej.2015.10.073.

[42] Han L, Liu Q, Lin K, Wang Q, Rong N, Liang X, et al. Enhanced hydrogen production via catalytic toluene reforming with in situ carbon dioxide capture: effects of a hybrid iron-calcium composite prepared by impregnation. Energy Convers Manag 2020;112834:214. https://doi.org/10.1016/j.enconman.2020.112834.

[43] Acha E, Chen D, Cambra JF. Comparison of novel olivine supported catalysts for high purity hydrogen production by CO_2 sorption enhanced steam reforming. J CO_2 Util 2020;101295:42. https://doi.org/10.1016/j.jcou.2020.101295.

[44] Sun H, Wang J, Zhao J, Shen B, Shi J, Huang J, et al. Dual functional catalytic materials of Ni over Ce-modified CaO sorbents for integrated CO_2 capture and conversion. Appl Catal B Environ 2019;244:63–75. https://doi.org/10.1016/j.apcatb.2018.11.040.

[45] Jing JY, Liu L, Xu K, Li WY. Improved hydrogen production performance of Ni–Al_2O_3/CaO–$CaZrO_3$ composite catalyst for CO_2 sorption enhanced CH_4/H_2O reforming. Int J Hydrogen Energy 2023;48:2558–70. https://doi.org/10.1016/j.ijhydene.2022.10.150.

[46] Vieira LM, Lima Santos DB, Hori CE. Bifunctional Ni–CaO catalysts modified with CeO_2 and inert $Ca_{12}Al_{14}O_{33}$ for sorption-enhanced steam reforming of ethanol. Int J Hydrogen Energy 2022;47:38556–70. https://doi.org/10.1016/j.ijhydene.2022.09.037.

[47] Wang N, Feng Y, Guo X, Ma S. Calcium-based pellets for continuous hydrogen production by sorption-enhanced steam methane reforming. Int J Hydrogen Energy 2024;49:897–909. https://doi.org/10.1016/j.ijhydene.2023.09.189.

[48] Landa L, Remiro A, Valecillos J, Valle B, Bilbao J, Gayubo AG. Unveiling the deactivation by coke of $NiAl_2O_4$ spinel derived catalysts in the bio-oil steam reforming: role of individual oxygenates. Fuel 2022;124009:321. https://doi.org/10.1016/j.fuel.2022.124009.

[49] Yan CF, Hu EY, Cai CL. Hydrogen production from bio-oil aqueous fraction with in situ carbon dioxide capture. Int J Hydrogen Energy 2010;35:2612–6. https://doi.org/10.1016/j.ijhydene.2009.04.016.

[50] Remiro A, Valle B, Aramburu B, Aguayo AT, Bilbao J, Gayubo AG. Steam reforming of the bio-oil aqueous fraction in a fluidized bed reactor with in situ CO_2 capture. Ind Eng Chem Res 2013;52:17087–98. https://doi.org/10.1021/ie4021705.

[51] Xie H, Yu Q, Zuo Z, Han Z, Yao X, Qin Q. Hydrogen production via sorption-enhanced catalytic steam reforming of bio-oil. Int J Hydrogen Energy 2016;41:2345–53. https://doi.org/10.1016/j.ijhydene.2015.12.156.

[52] Soria MA, Barros D, Madeira LM. Hydrogen production through steam reforming of bio-oils derived from biomass pyrolysis: thermodynamic analysis including in situ CO_2 and/or H_2 separation. Fuel 2019;244:184–95. https://doi.org/10.1016/j.fuel.2019.01.156.

[53] Landa L, Remiro A, Valecillos J, Valle B, Sun S, Wu C, et al. Sorption enhanced steam reforming (SESR) of raw bio-oil with Ni based catalysts: effect of sorbent type, catalyst support and sorbent/catalyst mass ratio. Fuel Process Technol 2023;107799:247. https://doi.org/10.1016/j.fuproc.2023.107799.

[54] Iliuta I, Desgagnés A, Yáñez Aulestia A, Pfeiffer H, Iliuta MC. Intensified bio-oil steam reforming for high-purity hydrogen production: numerical simulation and sorption kinetics. Int J Hydrogen Energy 2023;48:8783–806. https://doi.org/10.1016/j.ijhydene.2022.11.182.

[55] Gayubo AG, Valle B, Aramburu B, Montero C, Bilbao J. Kinetic model considering catalyst deactivation for the steam reforming of bio-oil over Ni/La_2O_3-αAl_2O_3. Chem Eng J 2018;332:192–204. https://doi.org/10.1016/j.cej.2017.09.063.

[56] Remiro A, Arandia A, Oar-Arteta L, Bilbao J, Gayubo AG. Regeneration of $NiAl_2O_4$ spinel type catalysts used in the reforming of raw bio-oil. Appl Catal B Environ 2018;237:353–65. https://doi.org/10.1016/j.apcatb.2018.06.005.

[57] Landa L, Valecillos J, Remiro A, Valle B, Bilbao J, Gayubo AG. Comparison of the $NiAl_2O_4$ derived catalyst deactivation in the steam reforming and sorption enhanced steam reforming of raw bio-oil in packed and fluidized-bed reactors. Chem Eng J 2023;141494:458. https://doi.org/10.1016/j.cej.2023.141494.

[58] Arandia A, Remiro A, Valle B, Bilbao J, Gayubo AG. Deactivation of Ni spinel derived catalyst during the oxidative steam reforming of raw bio-oil. Fuel 2020;117995:276. https://doi.org/10.1016/j.fuel.2020.117995.

[59] Valle B, García-Gómez N, Remiro A, Gayubo AG, Bilbao J. Cost-effective upgrading of biomass pyrolysis oil using activated dolomite as a basic catalyst. Fuel Process Technol 2019;106142:195. https://doi.org/10.1016/j.fuproc.2019.106142.

[60] Valle B, García-Gómez N, Remiro A, Bilbao J, Gayubo AG. Dual catalyst-sorbent role of dolomite in the steam reforming of raw bio-oil for producing H_2-rich syngas. Fuel Process Technol 2020;106316:200. https://doi.org/10.1016/j.fuproc.2019.106316.

[61] García-Gómez N, Valecillos J, Remiro A, Valle B, Bilbao J, Gayubo AG. Effect of reaction conditions on the deactivation by coke of a $NiAl_2O_4$ spinel derived catalyst in the steam reforming of bio-oil. Appl Catal B Environ 2021;120445:297. https://doi.org/10.1016/j.apcatb.2021.120445.

[62] García-Gómez N, Valle B, Valecillos J, Remiro A, Bilbao J, Gayubo AG. Feasibility of online pre-reforming step with dolomite for improving Ni spinel catalyst stability in the steam reforming of raw bio-oil. Fuel Process Technol 2021;106769:215. https://doi.org/10.1016/j.fuproc.2021.106769.

[63] Ochoa A, Aramburu B, Valle B, Resasco DE, Bilbao J, Gayubo AG, et al. Role of oxygenates and effect of operating conditions in the deactivation of a Ni supported catalyst during the steam reforming of bio-oil. Green Chem 2017;19:4315–33. https://doi.org/10.1039/c7gc01432e.

[64] Valle B, Aramburu B, Benito PL, Bilbao J, Gayubo AG. Biomass to hydrogen-rich gas via steam reforming of raw bio-oil over Ni/La_2O_3-αAl_2O_3 catalyst: effect of space-time and steam-to-carbon ratio. Fuel 2018;216:445–55. https://doi.org/10.1016/j.fuel.2017.11.151.

[65] Ochoa A, Valle B, Resasco DE, Bilbao J, Gayubo AG, Castaño P. Temperature programmed oxidation coupled with in situ techniques reveal the nature and location of coke deposited on a Ni/La_2O_3-αAl_2O_3 catalyst in the steam reforming of bio-oil. ChemCatChem 2018;10:2311–21. https://doi.org/10.1002/cctc.201701942.

[66] He L, Liao G, Hu S, Jiang L, Han H, Li H, et al. Effect of temperature on multiple competitive processes for co-production of carbon nanotubes and hydrogen during catalytic reforming of toluene. Fuel 2020;264. https://doi.org/10.1016/j.fuel.2019.116749.

[67] He L, Liao G, Li H, Ren Q, Hu S, Han H, et al. Evolution characteristics of different types of coke deposition during catalytic removal of biomass tar. J Energy Inst 2020;93:2497–504. https://doi.org/10.1016/j.joei.2020.08.009.

[68] Jiménez-González C, Boukha Z, de Rivas B, González-Velasco JR, Gutiérrez-Ortiz JI, López-Fonseca R. Behaviour of nickel–alumina spinel ($NiAl_2O_4$) catalysts for isooctane steam reforming. Int J Hydrogen Energy 2015;40:5281–8. https://doi.org/10.1016/j.ijhydene.2015.01.064.

[69] He L, Hu S, Jiang L, Liao G, Zhang L, Han H, et al. Co-production of hydrogen and carbon nanotubes from the decomposition/reforming of biomass-derived organics over Ni/α-Al_2O_3 catalyst: performance of different compounds. Fuel 2017;210:307–14. https://doi.org/10.1016/j.fuel.2017.08.080.

[70] Guil-Lopez R, Navarro RM, Ismail AA, Al-Sayari SA, Fierro JLG. Influence of Ni environment on the reactivity of Ni-Mg-Al catalysts for the acetone steam reforming reaction. Int J Hydrogen Energy 2015;40:5289–96. https://doi.org/10.1016/j.ijhydene.2015.01.159.

[71] Yang X, Weng Y, Li M, Sun B, Li Y, Wang Y. Enhanced hydrogen production by steam reforming of acetic acid over a Ni catalyst supported on mesoporous MgO. Energy Fuel 2016;30:2198–203. https://doi.org/10.1021/acs.energyfuels.5b02615.

[72] Sing KSW, Everett DH, Haul RAW, Moscou L, Pierotti RA, Rouquerol J, et al. Reporting physisorption data for Gas/Solid systems with special reference to the determination of surface area and porosity. Pure Appl Chem 1985;57:603–19. https://doi.org/10.1351/pac198557040603.

[73] Snoeck JW, Froment GF, Fowles M. Steam/CO_2 reforming of methane. Carbon filament formation by the boudouard reaction and gasification by CO_2, by H_2, and by steam: kinetic study. Ind Eng Chem Res 2002;41:4252–65. https://doi.org/10.1021/ie010666h.

[74] Brito J, Pinto F, Ferreira A, Soria MA, Madeira LM. Steam reforming of biomass gasification gas for hydrogen production: from thermodynamic analysis to experimental validation. Fuel Process Technol 2023;107859:250. https://doi.org/10.1016/j.fuproc.2023.107859.

[75] Cortazar M, Lopez G, Alvarez J, Amutio M, Bilbao J, Olazar M. Behaviour of primary catalysts in the biomass steam gasification in a fountain confined spouted bed. Fuel 2019;253:1446–56. https://doi.org/10.1016/j.fuel.2019.05.094.

[76] De Andrés JM, Narros A, Rodríguez ME. Behaviour of dolomite, olivine and alumina as primary catalysts in air–steam gasification of sewage sludge. Fuel 2011;90:521–7. https://doi.org/10.1016/j.fuel.2010.09.043.

[77] Arandia A, Remiro A, García V, Castaño P, Bilbao J, Gayubo AG. Oxidative steam reforming of raw bio-oil over supported and bulk Ni catalysts for hydrogen production. Catalysts 2018;322:8. https://doi.org/10.3390/catal8080322.

[78] Dang C, Xia H, Luo J, Cai W. Dendritic layered Ni/Al_2O_3 derived from $NiAl_2O_4$ as high-performance catalyst for dry reforming of methane. Fuel Process Technol 2023;107615:241. https://doi.org/10.1016/j.fuproc.2022.107615.

[79] Arregi A, Lopez G, Amutio M, Barbarias I, Santamaria L, Bilbao J, et al. Regenerability of a Ni catalyst in the catalytic steam reforming of biomass pyrolysis volatiles. J Ind Eng Chem 2018;68:69–78. https://doi.org/10.1016/j.jiec.2018.07.030.

[80] Barbarias I, Artetxe M, Lopez G, Arregi A, Santamaria L, Bilbao J, et al. Catalyst performance in the HDPE pyrolysis-peforming under reaction-regeneration cycles. Catalysts 2019;414:9. https://doi.org/10.3390/catal9050414.

[81] Rodríguez S, Capa A, García R, Chen D, Rubiera F, Pevida C, et al. Blends of bio-oil/biogas model compounds for high-purity H_2 production by sorption enhanced steam reforming (SESR): experimental study and energy analysis. Chem Eng J 2022;134396:432. https://doi.org/10.1016/j.cej.2021.134396.
[82] Wang G, Dai Y, Yang H, Xiong Q, Wang K, Zhou J, et al. A review of recent advances in biomass pyrolysis. Energy Fuel 2020;34:15557–78. https://doi.org/10.1021/acs.energyfuels.0c03107.
[83] Singh S, Pant KK, Krishania M. Current perspective for bio-oil production from agricultural residues in commercialization aspect: a review. J Anal Appl Pyrolysis 2023;106160:175. https://doi.org/10.1016/j.jaap.2023.106160.
[84] Ahmed SF, Rafa SJ, Mehjabin A, Tasannum N, Ahmed S, Mofijur M, et al. Bio-oil from microalgae: materials, production, technique, and future. Energy Rep 2023;10:3297–314. https://doi.org/10.1016/j.egyr.2023.09.068.
[85] Mendes FL, de Pinho AR, de Almeida MBB, Caramão EB. Biomass pyrolysis in a circulating fluidized bed reactor: evaluating two strategies for the reduction of oxygen content in bio-oil. J Anal Appl Pyrolysis 2023;106150:175. https://doi.org/10.1016/j.jaap.2023.106150.
[86] Shirzad M, Karimi M, Silva JAC, Rodrigues AE. Moving bed reactors: challenges and progress of experimental and theoretical studies in a century of research. Ind Eng Chem Res 2019;58:9179–98. https://doi.org/10.1021/acs.iecr.9b01136.
[87] Singh PP, Jaswal A, Singh R, Mondal T, Pant KK. Green hydrogen production from biomass – a thermodynamic assessment of the potential of conventional and advanced bio-oil steam reforming processes. Int J Hydrogen Energy 2024;50:627–39. https://doi.org/10.1016/j.ijhydene.2023.10.099.